Water Resources Research

RESEARCH ARTICLE
10.1029/2022WR033983

Representation of Fully Three-Dimensional Interfacial Curvature in Pore-Network Models

Luke M. Giudici[1], A. Qaseminejad Raeini[1], Martin J. Blunt[1], and Branko Bijeljic[1]

[1]Department of Earth Science and Engineering, Imperial College London, London, UK

Key Points:

- Quasi 2D representations of interfacial curvature present in network modeling of multiphase flow are extended to three dimensions
- A fully 3D representation of curvature is needed for network models to reproduce the behavior of direct simulations and experiments
- Correct predictions of trapping and relative permeability with network modeling rely on a physically accurate inclusion of curvature

Correspondence to:
L. M. Giudici,
luke.giudici@imperial.ac.uk

Citation:
Giudici, L. M., Qaseminejad Raeini, A., Blunt, M. J., & Bijeljic, B. (2023). Representation of fully three-dimensional interfacial curvature in pore-network models. *Water Resources Research*, *59*, e2022WR033983. https://doi.org/10.1029/2022WR033983

Received 27 OCT 2022
Accepted 17 MAR 2023

Abstract Quasi two-dimensional approximations of interfacial curvature, present in current network models of multiphase flow in porous media, are extended to three dimensions. The new expressions for threshold capillary pressure are validated and calibrated using high-resolution direct numerical simulations on synthetic geometries. The effects of pore-space expansion and sagittal interface curvature on displacement are quantified, and are shown to be a key step in improving the physical accuracy of network models. Finally, the calibrated network model is used to obtain predictions for relative permeability and capillary pressure in a water-wet Bentheimer sandstone. The predictions are compared to experimental measurements, revealing that the inclusion of three-dimensional interfacial curvature leads to more accurate predictions.

1. Introduction

Multiphase flow through permeable media is central to a variety of important practical problems and societal challenges including contaminant transport (Bear & Cheng, 2010; Essaid et al., 2015), capillary rise (Hall, 2009; Jorenush & Sepaskhah, 2003), carbon capture and storage (Alhosani et al., 2020; Boot-Handford et al., 2014; Krevor et al., 2015) and gas-water flow in polymer electrolyte membrane fuel cells (Mukherjee et al., 2011; Okonkwo & Otor, 2021; Zhang et al., 2021). Flow through permeable media is governed by the behavior of the fluids at the pore scale (Blunt, 2017). To address the aforementioned challenges, it is necessary to have a detailed representation of the media and a complete consideration of pore-scale physics, so that the most pertinent parameters can be accurately included into a numerical model. Recent advances in experimental methods and imaging (Wildenschild & Sheppard, 2013) have greatly improved the ability to describe geometry (Prodanović et al., 2007; Silin et al., 2011) and wettability (Andrew et al., 2014; Armstrong et al., 2012; Blunt et al., 2019; Sun et al., 2020) at the pore scale, yielding more accurate numerical model predictions (e.g., Akai et al., 2019; Foroughi et al., 2021; Ramstad et al., 2012). Whilst direct numerical simulations (DNS) on pore-space images are widely used to simulate flow through tens to hundreds of pores (e.g., Maes & Menke, 2021; McClure et al., 2021; Pan et al., 2004), the development of a computationally efficient model, which accurately captures pore-scale behavior through representative elementary volumes for complex systems, remains a crucial step toward achieving predictive capability for multiphase flow.

Pore-network models (PNMs), pioneered by Fatt (1956), offer the most feasible means to simulate flow through large samples efficiently. However, a key limitation to network modeling is the loss of physical detail caused by conceptualizing the pore space into idealized one, or two, dimensional shapes (Figure 1). Early PNMs represented the larger regions in the pore space, termed pores, and the connecting narrower restrictions, termed throats, by circular or cylindrical network elements (Figure 1b). Discretizing the pore space as a network of circular elements preserves the topology of a permeable medium and provides simple, semi-analytic expressions for fluid-fluid displacement (Chatzis & Dullien, 1977; Diaz et al., 1987), but renders it impossible to model flow through wetting layers present in the corners of the pore space (Figure 1a). Additionally, semi-analytic approximations are derived from a quasi one-dimensional system; the inscribed radius, r, is preserved, but all other detail in the axial (Figures 1e and 1f) and sagittal (Figures 1i and 1j) planes is lost.

To address these shortcomings, the advent of classical network models (CNM) saw the use of simple geometric shapes, such as triangles and squares (Bakke & Øren, 1997; Blunt, 1997), to represent the pores and throats of a medium with wetting layers present in its corners (Figure 1c). The classical approach maintains the efficiency and topology inherent to all network models, and has been used to reproduce upscaled flow properties in simple cases successfully (e.g., Lerdahl et al., 2000; Øren et al., 1998; Valvatne & Blunt, 2004). Despite improvements, classical approaches idealize the pore space as a quasi two-dimensional system—the axial plane (Figure 1g) solely

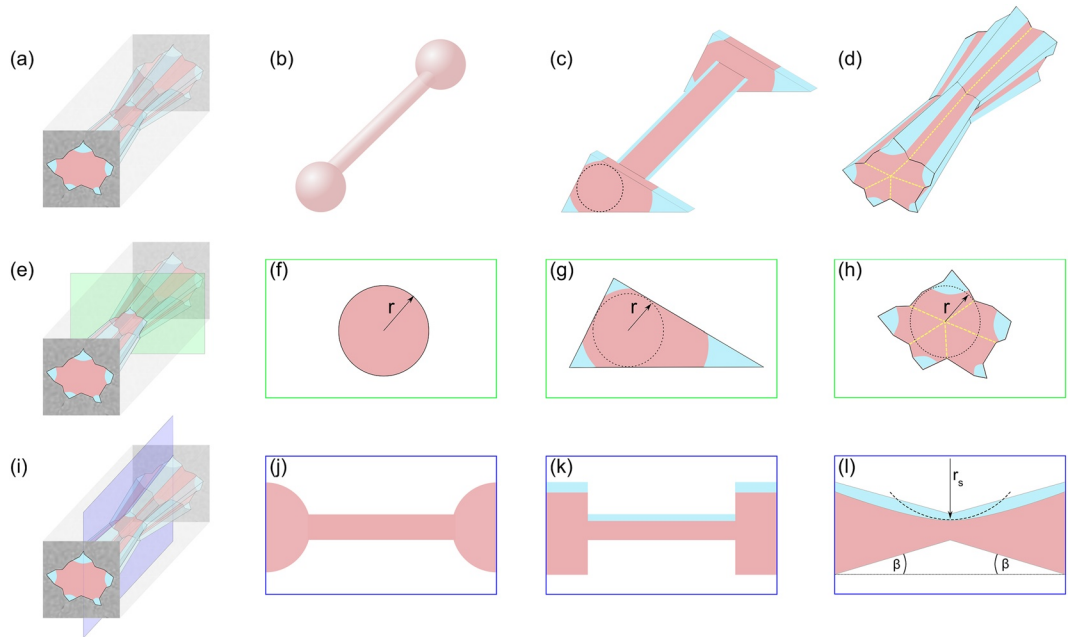

Figure 1. A schematic of a porous medium (a) and its axial (e) and sagittal (i) planes. The network representation of the medium using a variety of network extraction approaches is shown in (b)–(d). Early network models represented the pore space using circular elements (b), which preserve the inscribed radius of the pores and throats, r, and topology of the medium. However, circular elements do not preserve the corners of pore space in the axial plane (f), nor the geometry of the medium in the sagittal plane (j), and so the medium is modeled as a quasi one-dimensional system. The development of classical methods idealizes the pore space as simple shapes, such as triangles or squares (c). Simple shapes preserve corners in the axial plane (g) allowing wetting layers to be modeled, but neglect the geometry of the medium in the sagittal plane (k)—the network is merely a two-dimensional representation of the real, three-dimensional medium. The generalized network model (GNM) discretizes the medium using the corners of the pore space, shown by the dashed yellow lines in (d), which form the elements of the network. In the axial plane, the GNM preserves the number of corners present in the real medium (h). This work provides new formulations for the three-dimensional features preserved in the sagittal plane (l), namely the pore-space expansion (β) and the sagittal curvature (r_s) of layer interfaces.

provides the geometric detail used to derive semi-analytic approximations, whilst the geometry of the solid and the fluid-fluid interfaces in the sagittal plane are ignored (Figure 1k). This is a poor representation of multiphase flow through nearly all media, and direct numerical studies on synthetic media have shown that three-dimensional features present in the sagittal plane have a large impact on pore-scale flow (e.g., Deng et al., 2014; Rabbani et al., 2018). Furthermore, Bondino et al. (2013) showed that the classical elements themselves are non-unique and do not preserve the exact geometry of the underlying medium, leading to unreliable predictions. A solution to the shortcomings of classical approaches is a network model which captures the fully three-dimensional features of a real medium, with physical approximations that consider both the axial and the sagittal planes.

Figure 1d shows the generalized network model (GNM) (Raeini et al., 2017, 2018), which was developed to better discretize the geometry and connectivity of the pore space in three dimensions. In the axial plane, the GNM preserves the number of corners present in the underlying image (Figure 1h). The corners of the pore space form the elements of the network, which include all void-space voxels between two neighboring pores, shown in Figure 1d. Using the corners to discretize the pore space, it naturally follows that geometric detail in the sagittal plane can also be preserved (Figure 1l). To date, however, the precise formulations of pore-space expansion, β, and the sagittal curvature of fluid-fluid interfaces, r_s, in a network model have been largely unexplored. To obtain predictions truly representative of a real three-dimensional system, it is necessary to ensure that semi-analytic approximations correctly account for the effect of three-dimensional features on fluid-fluid interfaces.

In this work, the detailed geometry of the GNM is exploited to formulate the inclusion of pore-space expansion and the sagittal curvature of a fluid-fluid meniscus. To do this accurately, high-resolution direct simulations of two-phase flow through a variety of synthetic geometries and wettabilities, performed with a volume-of-fluid method, are used to calibrate GNM developments. The effect of pore-space expansion and sagittal curvature on

threshold pressures for displacement events are quantified from the volume-of-fluid simulations and compared to both generalized, and classical, network model predictions. A pressure dependence of sagittal curvature is revealed, with direct simulations used to further develop and calibrate pore-by-pore inclusion of three-dimensional effects into the GNM. Finally, the impact of physically accurate fluid interfaces on macroscopic two-phase flow parameters is demonstrated through a comparison with experimental results. Overall, the outcome is a pore-network model that accurately captures the full three-dimensional nature of fluid displacement, validated by direct pore-scale numerical simulation.

2. Methods

In Section 2.1, the GNM for multiphase flow is described and new representations of interfacial curvature—which extend quasi two-dimensional approximations to three-dimensions—are presented. In Section 2.2, the direct method used to validate GNM developments is detailed. Finally, in Section 2.3, the synthetic geometries, flow conditions and comparison methods used to validate GNM developments with direct simulations are explained.

2.1. The Generalized Network Model

The generalized network extraction algorithm (Raeini et al., 2017) is used to discretize the void space in a micro-CT image into individual pores and throats, which together form the elements of a network. Pore centers are defined as local maxima of the distance map—a scalar field representing the distance between a void voxel and its nearest solid voxel—while throat centers are defined as the restriction between two adjacent pores. Every void voxel in a micro-CT image is assigned to a unique pore and throat element, and the network as a whole preserves the topology of the pore space.

The throats, which include all voxels between two neighboring pore centers, are further divided along their medial axes into corners (Figure 1d). This discretization preserves a rich description of the pore space that is absent from classical network approaches, as the corners' geometric parameters are acquired directly from the underlying image. The single-phase permeability of the sample is preserved via an upscaling of the Navier-Stokes equations solved directly on the image.

Quasi-static, capillary dominated two-phase flow is simulated through the extracted network using the generalized network flow model (Raeini et al., 2018). After a user-defined change in network saturation, the conductivity of the corners comprising each throat is calculated and averaged to provide the conductivity of that throat. Subsequently, mass balance on each pore, p, is invoked to calculate the flow rate:

$$\sum_{t\in p} q_t^\alpha = \sum_{t\in p} g_t^\alpha (\Phi_p - \Phi_{nei}) = 0 \tag{1}$$

where q_t^α is the total flow rate of a phase (α) passing through a throat (t), g_t^α is the throat conductivity and $\Phi_p - \Phi_{nei}$ is the viscous pressure drop between neighboring pores. The summation is over all throats connected to a given pore.

Changes in network saturation are caused by displacements, which are driven by incrementally increasing the invading phase pressure at the inlet, with fluid interface locations updated in accordance with capillary equilibrium in each pore or throat:

$$P_c = P_1 - P_2 = \sigma\kappa \tag{2}$$

where P_c is the capillary pressure, P_1 and P_2 are the fluid pressures of the two phases, σ is the interfacial tension and κ is the total curvature of the interface. All simulations in this work are performed with $\sigma = 0.03\ \mathrm{Nm}^{-1}$ unless otherwise stated.

Accurate calculation of κ in Equation 2 is crucial to the correct prediction of threshold displacement pressures, which ultimately determine the saturation and hence the conductivity of the network. In the following sections, updated expressions for piston-like and layer curvature are presented, which extend classical quasi two-dimensional approximations to three dimensions. Methods to determine the new terms are then described.

2.1.1. Curvature for Piston-Like Advance

Traditionally, the curvature of a piston-like (terminal) meniscus is determined by considering an energy balance on the layer interfaces, termed arc-menisci, present in the corners of the pore space (Figure 1g). This is a

two-dimensional calculation which ignores curvature in the sagittal plane. With complex geometry the energy balance is algebraically elaborate to simplify, but the key result is that the total curvature is related to the ratio of the effective perimeter (P_{eff}) and area (A_{eff}) occupied by the invading phase, given by $\kappa = \frac{P_{eff}}{A_{eff}}\cos\theta$, where θ is the advancing or receding contact angle (Mason & Morrow, 1991). For classical networks—which use a shape factor, $G = \frac{A}{P^2}$, to represent the ratio of the total area (A) to the total perimeter (P)—the total curvature of a piston-like interface, κ_{pl}, is given by:

$$\kappa_{pl} = \frac{\cos\theta\left(1 + 2\sqrt{\pi G}\right)}{r} F_d(\theta, G, \gamma), \tag{3}$$

where F_d is a dimensionless correction factor accounting for the wetting layers retained in the corners, r is the inscribed radius of the element and γ represents the corner half-angles (Blunt, 2017).

While Equation 3 accounts for the effect of wetting layers on terminal meniscus curvature, and ensures capillary equilibrium between layer and piston-like interfaces, it does not include the three-dimensional effect that an expanding or contracting pore space has on the total curvature—Equation 3 is obtained purely from the axial plane shown in Figure 1g. Pore-space expansion has been shown to have considerable influence on entry pressures, particularly at neutral wettabilities with contact angles close to 90° (Rabbani et al., 2018). Therefore, if network models are to be truly predictive, they must include the expansion angle β, shown in Figure 1l. Raeini et al. (2018) proposed the following expression for piston-like curvature, for which the derivation and the definition of terms are presented in Appendix A:

$$\kappa_{pl} = \frac{\sum_{c\in t}(2h_l\cos(\theta+\beta) + W_l\hat{\mathbf{s}}\cdot\hat{\mathbf{x}})}{A_{total} - A_{layer}}, \tag{4}$$

where the summation is performed over every corner (c) belonging to a throat (t). Here, a method to determine β on a pore-by-pore basis is presented.

Consider Figure 2, which shows a pore and two possible connectivity scenarios, with a piston-like interface present in the left-most throat. As the pressure of the red, invading phase increases, the fluid-fluid interface will displace into the pore center with a curvature given by Equation 4. However, the angle β is not necessarily constant—it can vary depending on the exact geometry and topology of the local pore space. Two vectors are defined, $\mathbf{p}$ and $\mathbf{t}$, which point from the occupied throat center to the pore center and the adjacent throat center, respectively.

The vectors $\mathbf{p}$ and $\mathbf{t}$ are used to produce an empirical expression to approximate β, in every corner, at three locations: $x_{pl} = \left\{0, \frac{1}{2}, 1\right\}$, where x_{pl} is the fractional distance from throat center to pore center. The empirical expression approximates the solid wall as sinusoidal and accounts for connected throats:

$$\beta = \tan^{-1}\left(\frac{a\sin(\pi x_{pl})(r_p - r_t)}{D}\right) + b\sin\left(\frac{\pi}{2}x_{pl}\right)\cos^{-1}\left(\frac{\mathbf{t}\cdot\mathbf{p}}{\|\mathbf{t}\|\|\mathbf{p}\|}\right), \tag{5}$$

where r_p and r_t are the pore and throat radii, respectively, and D is the distance between pore center and throat center. The coefficients a and b are sensitivity parameters and are set to 0.3 and 1.1 in this work, respectively: the reader is referred to Figure C1 for further details on how these values are determined. If a corner's neighboring throat is situated exactly opposite the current throat, shown schematically in Figure 2a and in cross-section in Figure 2c, the dot product of $\mathbf{p}$ and $\mathbf{t}$ is zero and Equation 5 reduces to the first term—a simple trigonometric expression modulated by the sine function. However, if other adjacent throats are present (Figure 2b), the second term in Equation 5 accounts for additional expansion shown in Figure 2d, where the expansion angle β is greatest at the pore center.

The performance of Equation 5 is evaluated against volume-of-fluid simulations of piston-like advance through a wide range of wettabilities, which will be explained further in Section 2.3.1.

2.1.2. Layer Sagittal Curvature

The total fluid-fluid curvature present in Equation 2 represents the sum of the principal components of curvature, κ_a and κ_s, of the interface:

$$\kappa = \kappa_a + \kappa_s. \tag{6}$$

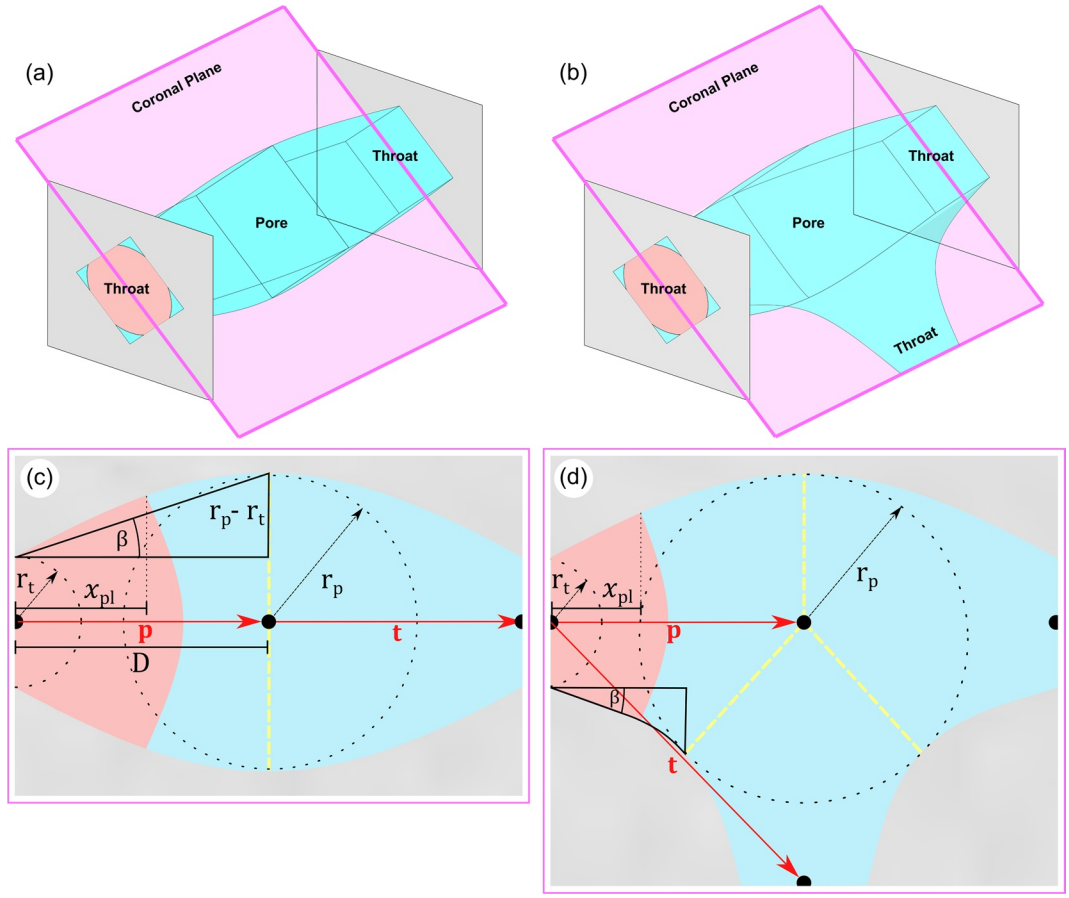

Figure 2. A schematic showing the parameters used to determine the expansion angle, β, at which the solid is inclined to the line connecting throat and pore center. In a pore-throat arrangement where the throats are exactly opposite one another, as shown in (a), β is determined using the difference in pore (r_p) and throat (r_t) radii, as well as the pore-throat distance, D, which are shown in the coronal-plane cross-section in (c). However, if the throats connecting to a pore are not opposite each other—shown schematically in (b)—it is assumed that β will take a maximum value at the pore center and an additional correction must be included. The correction uses the dot product of the vectors connecting the throat to the pore center (**p**) and to the adjacent throat center (**t**), shown in the coronal-plane cross-section in (d). In both cases, the solid wall is modeled as sinusoidal, and estimates are taken at a distance $x_{pl} = \left\{0, \frac{1}{2}, 1\right\}$, where x_{pl} is the fractional distance from pore to throat.

For piston-like interfaces, κ can be determined from a force balance on the interface, as previously shown in Equation 4. For layer configurations, however, a force balance becomes more complex. Therefore, it is typical in network modeling to assume that the second principal component of curvature—termed here as the sagittal curvature (κ_s)—is negligible, and so the total curvature is equal to the curvature in the axial plane, $\kappa = \kappa_a$. Strictly speaking, this assumption is only valid for a system which can be approximated as infinitely long and radially invariant, such as a capillary tube of constant radius (Lenormand et al., 1983). As discussed previously, many studies have noted that, in truly three-dimensional geometries, curvature in the sagittal plane affects capillary pressure predictions (e.g., Deng et al., 2014; Raeini et al., 2014). To date, however, only one network model has attempted to include sagittal curvature (Raeini et al., 2018). Below, a new approach for incorporating sagittal curvature into a network model on a pore-by-pore basis is provided.

Consider Figure 3, which schematically shows the sagittal plane (Figure 1i) of a throat (a) and a pore (b). It is evident from Figure 3 that the curvature of the wetting layers in the sagittal plane is not zero. To approximate it, the corner vertices at every throat center are assumed to be a local origin, O. Then, a set of vectors are defined dependent upon whether the sagittal curvature at a throat or at a pore is to be calculated. At a throat center, two edge vectors between the throat corner vertices and the neighboring pore corner vertices, $\mathbf{e_1}$ and $\mathbf{e_2}$, are defined (Figure 3a). Provided that O, $\mathbf{e_1}$, and $\mathbf{e_2}$ are non-colinear, these three points are sufficient to define a unique circle with radius r_{st} in the sagittal plane. The center of this circle, $\mathbf{C_{st}}$, is determined from the intersection of the vectors

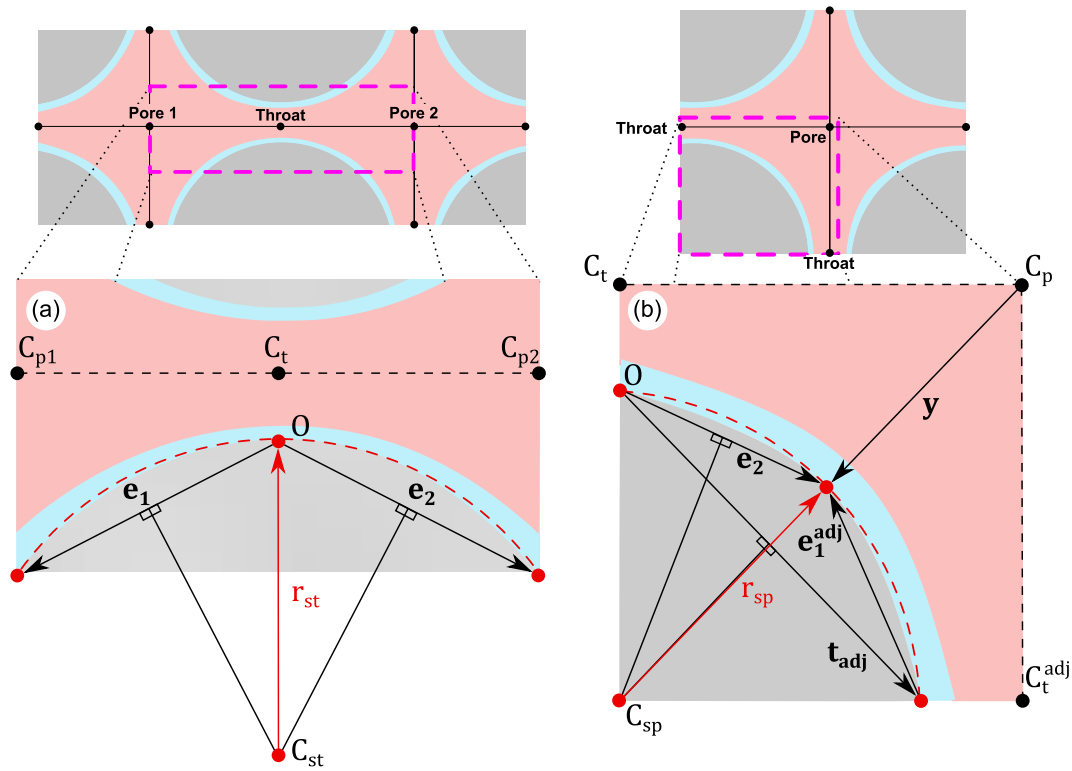

Figure 3. A schematic showing the method used to determine the radius of sagittal curvature, r_s, of a layer at a throat (a) and at a pore (b). In (a), the radius of sagittal curvature at the throat (r_{st}) is defined using the circle formed by the throat corner, O, and the two edge vectors $\mathbf{e_1}$ and $\mathbf{e_2}$, which are the position vectors of the neighboring pore corners relative to O. In (b), the radius of sagittal curvature at the pore (r_{sp}) is obtained from the circle defined by O, $\mathbf{e_2}$ and the position vector of the neighboring throat corner, $\mathbf{t_{adj}}$, relative to O. In addition, the sign of r_{sp} is determined by the dot product of the sum of the adjacent throat's edge vector, $\mathbf{e}_1^{adj}$, and $\mathbf{e_2}$ with the pore-center to pore-corner axis, $\mathbf{y}$.

normal to $\mathbf{e_1}$ and $\mathbf{e_2}$. Subsequently, the sagittal curvature at the throat, κ_{st}, is assumed to be inversely proportional to r_{st}—which is calculated as the distance between the throat corner vertex and $\mathbf{C_{st}}$—and is always negative:

$$\kappa_{st} = -\frac{c}{r_{st}} = -\frac{c}{|\mathbf{C_{st}}|}. \tag{7}$$

For pore centers, the edge vector $\mathbf{e_2}$ and the vector between adjacent throat corner vertices, $\mathbf{t_{adj}}$, establish the three points needed to determine the circle defining the pore sagittal curvature, which has a radius r_{sp} and center $\mathbf{C_{sp}}$ (Figure 3b). Additionally, the adjacent throat's edge vector, $\mathbf{e}_1^{adj}$, and the pore-center to pore-corner axis, $\mathbf{y}$, are needed to determine the sign of the pore sagittal curvature:

$$\kappa_{sp} = \begin{cases} \dfrac{d}{r_{sp}} = \dfrac{d}{|\mathbf{C_{sp}}|}, & \text{if } \left(\hat{\mathbf{e}}_2 + \hat{\mathbf{e}}_1^{adj}\right) \cdot \hat{\mathbf{y}} > 0 \\ -\dfrac{d}{r_{sp}} = -\dfrac{d}{|\mathbf{C_{sp}}|}, & \text{otherwise.} \end{cases} \tag{8}$$

The generalized network represents a coarse-scale discretization of the porous medium, from which only a finite set of vertices may be used to calculate sagittal curvature. In reality, curvature is mathematically defined at an infinitesimal portion of a fluid interface (Blunt, 2017). The coefficients c and d in Equations 7 and 8 therefore represent calibration factors which account for the coarse discretization in the GNM, and are used to optimize the approximation of sagittal curvature.

Equations 7 and 8 are used to define the sagittal curvature at every pore and throat center of each corner in the network, prior to initiating fluid injection. In the following, the direct numerical simulation method used to assess and calibrate Equations 5, 7, and 8 is explained.

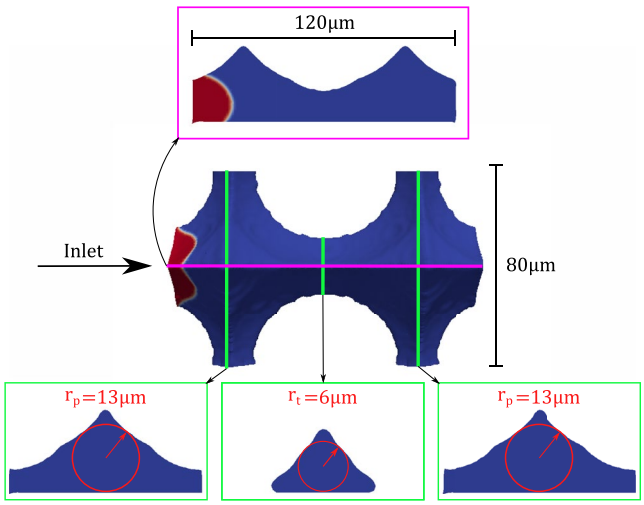

Figure 4. The dimensions of the synthetic two-pore geometry used in the analysis of piston-like curvature. The magenta line represents a sagittal plane of the system, shown in cross-section in the top of the figure, while the green lines show axial planes at the pore and throat centers, shown in cross-section at the bottom of the figure. The pore and throat radii are denoted by r_p and r_t, respectively. The two-pore system is initialized with a 5% saturation of invading (red) fluid before injection commences.

2.2. Volume of Fluid Method

The essential details of the direct method are outlined here—for a complete treatment the reader is referred to Raeini et al. (2012) and Shams et al. (2018). All differential equations that follow are solved using the OpenFOAM finite volume library (Jasak et al., 2007).

The flow of two isothermal, incompressible and immsicible Newtonian fluids is described by the set of Navier-Stokes equations:

$$\nabla \cdot \mathbf{u} = 0 \tag{9}$$

$$\frac{D}{Dt}(\rho \mathbf{u}) - \nabla \cdot \mathbb{T} = -\nabla p + \mathbf{F} + \mathbf{f}_c. \tag{10}$$

The velocity field, $\mathbf{u}$, is updated based upon the pressure gradient, ∇p, the body forces acting on the fluid, $\mathbf{F}$, and the capillary force, $\mathbf{f}_c$, which is determined through the contour-level surface force model (Shams et al., 2018). The viscous stress tensor is denoted as $\mathbb{T} = \mu\left(\nabla \mathbf{u} + (\nabla \mathbf{u})^T\right)$, where μ is the dynamic viscosity.

The two fluids are treated as a single fluid-continuum system, with an indicator function, α defined throughout the flow domain representing the volume fraction of the phases in each grid cell. The indicator function is a continuous variable $\alpha = [0, 1]$, taking a value $\alpha = 1$ if the cell is completely filled with phase 1 and a value $\alpha = 0$ if the cell is filled with phase 2. Values between zero and one are present in cells containing the fluid-fluid interface, which is tracked and evolved using the advection equation:

$$\frac{\partial \alpha}{\partial t} + \nabla \cdot (\alpha \mathbf{u}) = 0. \tag{11}$$

The density and viscosity of the fluids is 1,000 kgm^{-3} and 0.001 Pas, respectively. All simulations are capillary dominated, with a capillary number, $C_a = \frac{\mu q}{\sigma}$, of 6.67×10^{-6} for the injected phase, where q represents the Darcy velocity. The contour-level surface force model used in this work significantly enhances the accuracy of capillary pressure predictions (Shams et al., 2018). The mesh discretizing the flow domain is unstructured, with cubic grid blocks in the center and grid blocks deformed to align with the solid walls at the boundaries. The resolution is 1 µm per grid block, with an extra layer of cells added near the solid walls to more accurately capture wetting layers.

The volume-of-fluid method is used to simulate piston-like advance and layer growth in synthetic geometries, with the predictions compared to those obtained with network modeling. The following section describes the geometries, flow conditions and methods used to compare and validate the network model developments presented in Section 2.1 with volume-of-fluid simulation predictions.

2.3. Synthetic Geometries, Flow Conditions and Comparison

The geometry and related flow conditions considered depend upon the local property being analyzed. Below, the properties of interest are separated and their respective flow conditions and points of comparison are described.

2.3.1. Piston-Like Curvature Analysis

To analyze piston-like curvature, a synthetic two-pore system is constructed using intersecting spheres. To save time, the symmetry of the system is exploited by a lengthways bisection. The synthetic geometry and its dimensions are shown in Figure 4.

Using the volume-of-fluid method, a piston-like interface is initialized at the inlet side of the two-pore system, corresponding to an initial invading fluid saturation of 5%. Subsequently, the wettability is assigned and the invading phase is injected to simulate piston-like advance of the terminal meniscus. The range of contact angles,

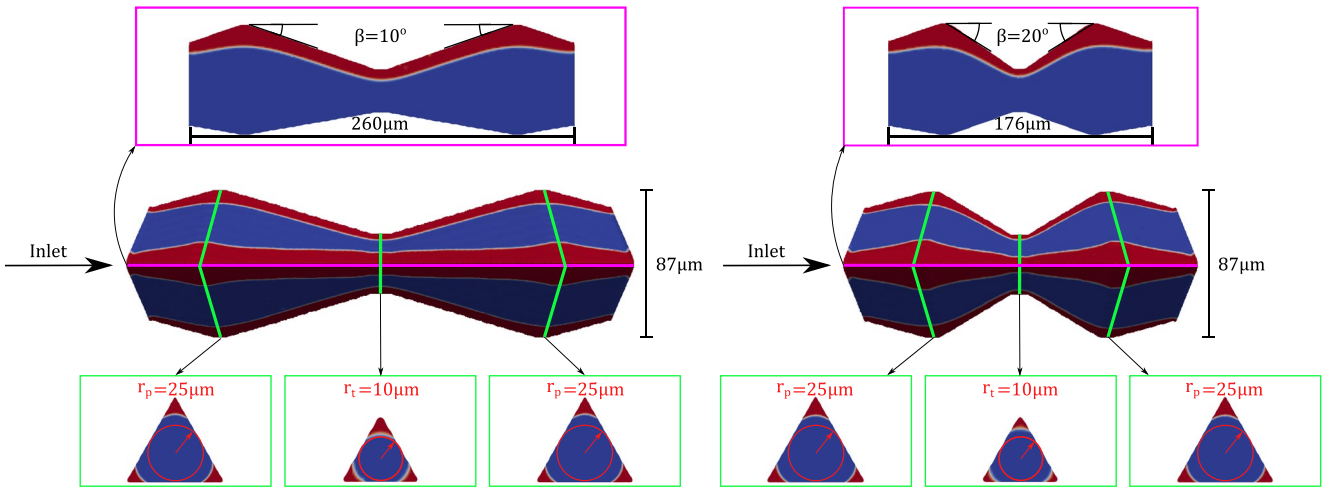

Figure 5. The dimensions of the equilateral triangular geometries used in the analysis of layer growth. The two geometries' axial planes at the pore and throat centers are highlighted in green, shown in cross-section at the bottom of the figure. In the axial planes, the pore and throat radii are denoted by r_p and r_t, respectively, and the geometries are axially identical. However, the sagittal planes, in magenta, are different—the left geometry has an expansion angle of $\beta = 10°$, shown in the upper left sagittal curvature cross-section, while the right geometry has $\beta = 20°$, shown in the upper right cross-section. Note that, due to the symmetry of the system, only one sagittal plane of each geometry is shown, while in reality each corner has its own sagittal plane.

measured through the receding phase, used for the simulations of piston-like advance span from 30° to 150° in 15° increments. This wide selection of contact angles covers drainage, imbibition and neutral wettabilities.

Separately, the GNM is used to extract a network from the geometry in Figure 4 and to simulate piston-like advance for the same range of contact angles as in the volume-of-fluid simulations. The maximum capillary pressure necessary to reach the outlet is compared between the two model predictions, in addition to the capillary pressure needed to occupy the center of the throat and each neighboring pore. The capillary pressure is defined by Equation 2, where the invading phase corresponds to phase 1.

2.3.2. Analysis of Layer Sagittal Curvature

In the analysis of three-dimensional layer configurations and their effect on capillary pressure, the property of interest is the deviation of total curvature predictions from two-dimensional analytic predictions for layer curvature, which is derived for a general corner angle in Appendix B. To measure this deviation precisely, two equilateral triangular geometries are used which expand and contract with a user-defined expansion angle, β, set to $\beta = 10°$ and 20° in this work. The pore and throat radii are kept constant at 25 and 10 voxels respectively, resulting in a pore-throat contraction ratio of 2.5. The contact angle is kept at $\theta = 30°$, measured through the invading phase. Figure 5 shows the two geometries and their dimensions.

The generalized extraction algorithm is used to discretize the corners of the samples shown in Figure 5 and to obtain the generalized network geometries. In the volume-of-fluid simulations performed on the triangular geometries, layers are initialized in the corners of the pore space at an initial wetting phase saturation, S_w, of 14% and 12% for the 10° and 20° geometries, respectively. Subsequently, imbibition is simulated through the samples using the GNM and volume-of-fluid methods detailed previously, where the invading phase pressure now corresponds to phase 2 in Equation 2.

The model predictions for the threshold total curvature (capillary pressure) at which snap-off occurs, as well as the evolution of the principal components of curvature (Equation 6) as a function of saturation, are compared at the throat. To obtain the principal components of curvature from the volume-of-fluid simulation, Appendix B is used to determine the curvature in the axial plane at each time step. The axial curvature is then subtracted from the predicted total curvature to provide the sagittal curvature (Equation 6).

3. Results and Discussion

In Section 3.1 the local effect of implementing pore-space expansion and sagittal curvature, described in Sections 2.1.1 and 2.1.2, respectively, on threshold pressures for displacement is analyzed. Subsequently, the

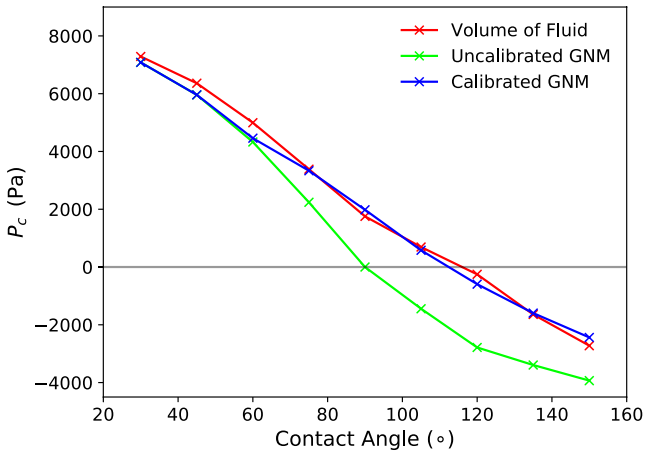

Figure 6. The threshold capillary pressure (P_c) needed to pass through the two-pore geometry shown in Figure 4 as a function of receding phase contact angle (θ). The red line shows the volume-of-fluid predictions, while the green and blue lines show the GNM predictions before and after implementing Equation 5, respectively.

impact of the local parameters on macroscopic relative permeabilities and capillary pressures is presented and discussed in Section 3.2. Finally, in Section 3.3, the computational cost of including a three-dimensional representation of interfacial curvature in network models is addressed.

3.1. Local Parameters

3.1.1. Pore-Space Expansion

Fundamentally, the displacement of one phase by another is a thermodynamic process (Morrow, 1970): displacement will only occur if it is energetically favorable. Displacements control the local configuration of the two fluids in the pore space, which upscales to the averaged macroscopic parameters used for predictions. Therefore, if the threshold pressures for displacements are predicted well, the upscaled predictions can inherit high accuracy.

Figure 6 shows the predicted threshold capillary pressures needed to pass through the two-pore system (Figure 4) using the volume-of-fluid method, the GNM prior to improvements, and the calibrated GNM after implementing the updated method for pore-space expansion described in Section 2.1.1.

The difference in threshold predictions between the volume-of-fluid method and the GNM prior to improvements is substantial. To quantify the difference, a dimensionless discrepancy, $\Delta P_c = \frac{r_t}{2\sigma}\left|P_c^{VoF} - P_c^{GNM}\right|$, is defined where P_c^{VoF} and P_c^{GNM} are the capillary pressures predicted by the volume-of-fluid method and the GNM, respectively, for any given contact angle and $r_t = 6$ μm is the inscribed radius of the throat in Figure 4. At the smallest contact angles ($\theta < 75°$) ΔP_c is below 0.1, while at intermediate and larger angles ($\theta \geq 75°$) ΔP_c is significantly greater and exceeds 0.2. However, the apparent wettability predicted by the two models offers the most insight into the physical nature of displacement at the pore scale: the volume-of-fluid method predicts $P_c > 0$ for all contact angles less than 120°, indicating that the invading fluid must be forced through the sample as the non-wetting phase. In the uncalibrated GNM, all wettabilities below $\theta = 90°$ are considered non-wetting to the invading phase, while all above are considered wetting. Exactly at 90°, the capillary pressure is zero, where displacement is driven by cooperative pore-body filling.

A zero capillary pressure at $\theta = 90°$ is an inevitable prediction from network models neglecting the expansion and contraction of the pore space in the sagittal plane, as the cosine term in Equation 3 becomes zero. Indeed, using Equation 3, one can erroneously infer a wetting system, with $P_c < 0$, for all $\theta > 90°$, as shown by the uncalibrated GNM in Figure 6. In reality, this is often incorrect—the apparent wettability of a system depends on the expansion angle of the solid surface in addition to the contact angle (Rabbani et al., 2018). The reason for this dependency becomes clear when considering the forces acting on an interface: in an inclined geometry, the balance of fluid-solid and fluid-fluid interfacial tensions acting at the three-phase contact line gives a contact angle through the Young equation (Hassanizadeh & Gray, 1993), however the direction of the fluid-fluid interfacial tension is further inclined from the flow direction by the angle β (Figure A1b). This gives rise to a different curvature, and hence apparent wettability, of the interface as compared to a geometry in which the solid walls are assumed parallel in the sagittal plane (Figure 1k). The effect of an inclined surface, in terms of the macroscopic volume-of-fluid predictions shown in Figure 6, is that the fluid interface maintains a positive curvature far above $\theta = 90°$, and is apparently non-wetting even at weakly wetting contact angles. After implementing Equation 5 with optimized coefficients obtained from Figure C1, the calibrated GNM correctly accounts for the impact β has on capillary pressure, accurately reproducing the behavior predicted by the direct method and reducing the absolute difference in predicted threshold capillary pressure by at least 1,500 Pa for all $\theta > 75°$. More insights into the nature of displacement at the pore scale can be obtained by analyzing the capillary pressure of the interface as it passes through the center of each pore and the connecting throat, rather than the threshold of the system as a whole.

Figure 7 shows the predicted capillary pressure of the interface as it passes through both pores and the middle throat, for the complete range of contact angles simulated. In pore-scale studies, it is common to attribute the macroscopic thresholds for displacement, shown in Figure 6, to the conceptualized pores and throats of a network—during drainage the most difficult step is considered to be invading the center of the narrowest

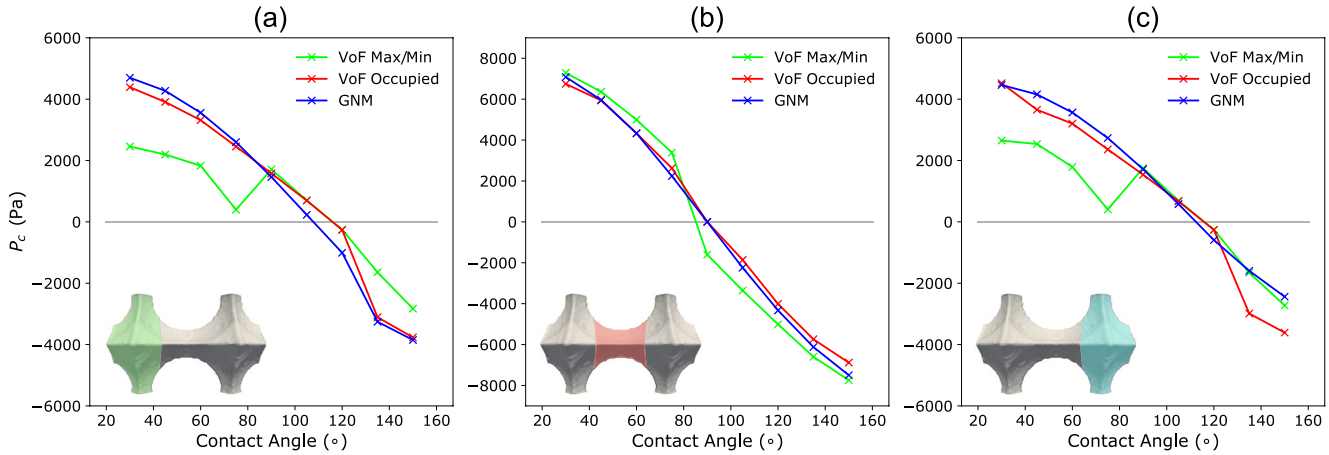

Figure 7. The local capillary pressure (P_c) predicted for each pore (a) and (c) and the adjoining throat (b) in Figure 4, as a function of receding phase contact angle (θ). In the green line, the maximum capillary pressure throughout the volume-of-fluid simulations is attributed to the throat, while the minimum is attributed to the pores, for $\theta < 90°$, and vice-versa for $\theta \geq 90°$. In blue, the generalized network P_c for pore and throat centers is shown. In red, the volume-of-fluid P_c is presented at the time when the pore or throat center is first occupied with the invading phase.

region (the throat center), while during imbibition it is the center of the widest regions (the pore centers) which offer most resistance to displacement (Blunt, 2017). Indeed, network model threshold entry pressures are almost always determined by considering only pore and throat centers. Using this convention, the GNM predictions at the throat center (Figure 7b) agree well with the volume-of-fluid thresholds, with some disagreement in the intermediate contact angle ranges (Figure 7b). The pores, however, show far greater disagreement, particularly during drainage where ΔP_c exceeds 0.25 in places (Figures 7a and 7c). The principal reason for this difference is that, if the expansion in the sagittal plane permits, $\cos(\theta + \beta)$ in Equation 4 can take a maximum or minimum value away from the pore and throat centers. This has been studied for neutral wettabilities (e.g., Pavuluri et al., 2020), but here the effect is seen even for relatively low and high contact angles.

Figure 8 shows the distance of the interfaces, at the threshold maxima and minima shown in Figure 7, from the throat center. At the lowest contact angles, the conventional assumption that the maximum capillary pressure is at the throat center, while the minimum is at the pore centers, is approximately correct, with only minor deviations. However, as the contact angle increases, the location of maxima and minima changes smoothly—the minima move toward the throat center, while the maxima move toward the pore center. At the highest contact angles, the invading phase is wetting, and the expected behavior of pore centers representing local maxima and throat centers local minima is again approximately correct. Interestingly, at $\theta = 105°$, the interface location of the P_c maxima reaches its greatest distance from the throat center, before decreasing at larger contact angles. This inflexion point marks the transition to imbibition—beyond $\theta = 105°$, the contact angle has increased to such an extent that $\cos(\theta + \beta)$ is negative, and so the total curvature becomes negative (Figure 6) with the defending phase protruding into the invading phase, moving the interface center toward the throat. In summary, the assumption that local minima and maxima are exactly at the pore and throat centers is likely only true for very low or very high contact angles, where small additions will not have much effect on the cosine function, or where β is very small. The better agreement of threshold pressures in the throats in Figure 7b can be attributed, in part, to a far smaller β than in the pores.

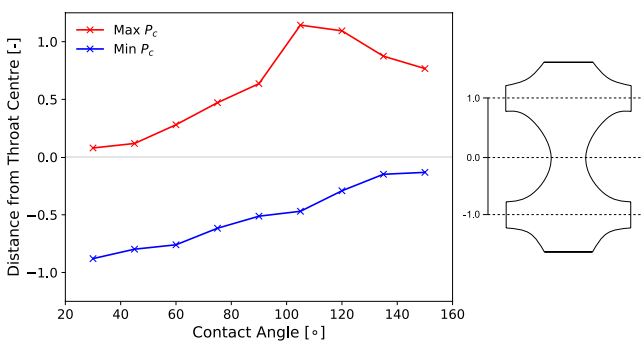

Figure 8. The fractional distance from throat center to pore center (right schematic) of the interface center position as a function of receding phase contact angle (θ). In blue, the interface position at minimum capillary pressure is shown, while red represents the position at maximum capillary pressure.

In the GNM, the threshold pressure for displacement is taken as the local maximum calculated from three, rather than two, locations: the pore center, the throat center, and the half-way point (Equation 5). For this reason, the large pore discrepancies seen in Figures 7a and 7c at low contact angles, and the relatively larger throat discrepancies at intermediate contact angles in Figure 7b, are not reflected in the macroscopic predictions in Figure 6—the GNM correctly identifies when the throat or half-way point becomes a local maximum and selects the appropriate threshold capillary pressure for

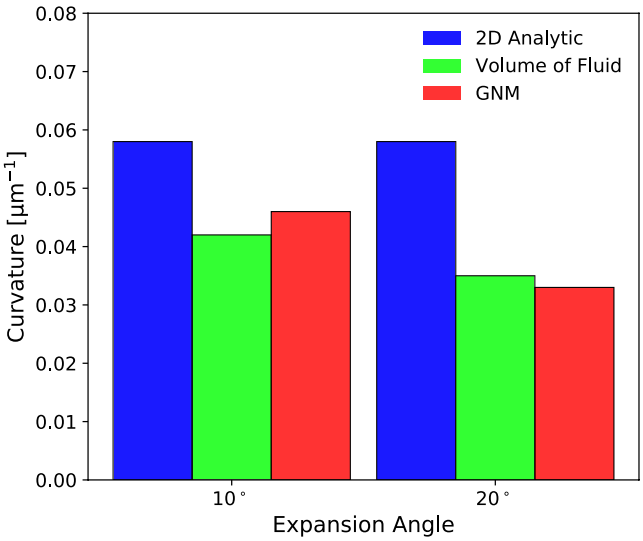

Figure 9. The predicted total curvature at which snap off occurs for the classical, two-dimensional approach (blue), the volume-of-fluid method (green) and the GNM after implementing sagittal curvature described in Section 2.1.2 (red).

displacement. Similarly, at wetting contact angles ($\theta > 105°$), where the pore centers control the threshold pressure for displacement and β reaches its maximum value, the calibrated GNM performs well, particularly at the macroscopic scale (Figure 6).

The exact nature of pore-filling is an interesting area of future research (Ruspini et al., 2017) and quickly becomes complex due to the presence of connected throats and the spontaneous formation of layers in wetting regimes, which alter the effective area of the interface (Equation A1). It is possible, however, to gauge the current accuracy of GNM capillary pressure estimates at the pore centers: Figure 7 also shows the volume-of-fluid capillary pressure predictions when the pores and throats first become occupied—that is, when the centers of the maximal balls defining the pore and throat centers first become filled with the invading phase. The network model agrees well with the direct method here, further validating that the capillary pressure estimates from Equation 4 and the updated β in Equation 5 are accurate.

3.1.2. Layer Sagittal Curvature and Snap-Off

The expansion and contraction of the pore space is clearly an important factor in piston-like displacement, but in this section it is shown that the three-dimensional nature of real porous media must also be considered for layer configurations. For any porous medium with corners and crevices to its pore space, wetting layers will maintain connectivity even after the centers of the pores and throats have been invaded by a non-wetting phase. If the wetting fluid is re-injected, the layers will swell until the interfaces from two neighboring corners meet. At this point, which first occurs in the narrowest regions of the pore space, the fluid configuration becomes unstable and the wetting phase rapidly fills the small region. This is the snap-off process, which acts to disconnect and trap the defending, non-wetting fluid, and has important implications for many two-phase flow processes. Therefore, correctly predicting the pressure and saturation at which snap-off occurs is crucial.

Figure 9 shows the predicted total curvature for snap-off, using a variety of approaches, for the 10° and 20° expansion geometries shown in Figure 5. The curvature of a layer interface in the axial plane with an arbitrary fluid-solid contact length is derived in Appendix B. Classical network models rely solely on analytic solutions to Equation B1 when calculating the total curvature at which the three-phase contact point of two adjacent corners in a throat will meet, and if the prevailing capillary pressure equals this critical value before a piston-like interface has reached the throat, snap-off will occur. The two-dimensional analytic prediction clearly overestimates the curvature at which snap-off occurs compared to the volume-of-fluid predictions. In addition, the classical approach predicts the same critical curvature value in both geometries, while the volume-of-fluid method predicts a decrease in the critical curvature with increasing expansion angle. The physical meaning of this is that, in classical networks, snap-off will occur at lower wetting saturations, or equivalently higher non-wetting residual saturations, than in reality. Moreover, if two pore geometries are identical in their axial planes, but vary in their sagittal planes—as in Figure 5—the predicted snap-off curvature in the two media will be the same. The sole cause of this predictive inaccuracy is the classical assumption that curvature in the sagittal plane is negligible and does not contribute to the total curvature of a layer interface. In reality, fluid layers conform to the geometry of the pore space, which expands away from throat centers. In the sagittal plane, the geometric constraint of an expanding medium results in fluid layers protruding into the center fluid, with a negative curvature, at the throat. This was shown schematically in Figure 11 and was shown in cross-sections from direct simulations in Figure 5. From Equation 6, a negative sagittal curvature reduces the total curvature, or capillary pressure, needed to achieve a given axial curvature—snap-off becomes more difficult with increasing throat sagittal curvature, as predicted by the volume-of-fluid method in Figure 9.

After including throat sagittal curvature, as in Equation 7 and with the optimized coefficient $c = 1.5$ (Figure C2a), the GNM accurately predicts both the lower critical curvatures than analytic solutions and the variation between expansion angles shown by the volume-of-fluid simulations. However, underpinning the approach used in Section 2.1.2, and indeed other approaches (Deng et al., 2014; Raeini et al., 2018), is the assumption that sagittal curvature is defined solely by the geometry and is not a function of pressure. For a truly predictive model it is not sufficient to only predict the threshold curvature for snap-off, based purely on pore-space geometry—the effect

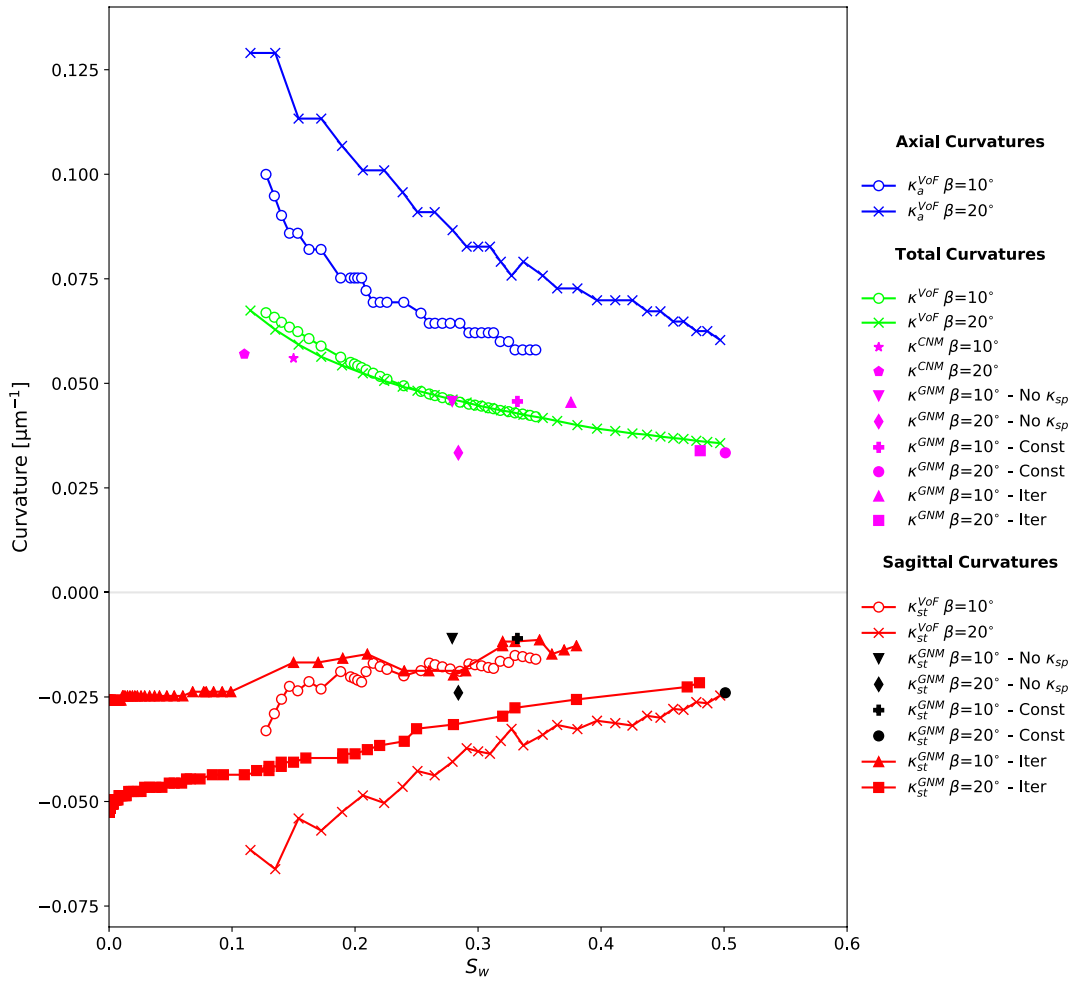

Figure 10. Curvature at the throat center as a function of wetting phase saturation S_w, for the $\beta = 10°$ and $\beta = 20°$ geometries shown in Figure 5, for a contact angle of 30° through the wetting layer. The total curvatures from the volume-of-fluid simulations are shown in green (κ^{VoF}), while the axial curvatures obtained using Equation B1 throughout the volume-of-fluid simulations are shown in blue $\left(\kappa_a^{VoF}\right)$. The difference between κ_a^{VoF} and κ^{VoF} gives the sagittal curvature, shown in red $\left(\kappa_{st}^{VoF}\right)$. In each case, the end point represents the value at snap-off. The magenta symbols represent the total curvature at snap-off obtained with the GNM when: no sagittal curvature is considered, as in classical network models (κ^{CNM}); only constant throat sagittal curvature is considered (κ^{GNM} - No κ_{sp}); constant pore and throat sagittal curvatures are considered (κ^{GNM} - Const). The sagittal curvatures at snap-off associated with the total curvatures obtained using the GNM are shown by the black symbols. Finally, the GNM predictions for sagittal curvature after implementing the iterative method in Figure 11 (κ_{st}^{GNM} - Iter) are shown in red, with the associated GNM total curvature predictions for snap-off shown by magenta symbols (κ^{GNM} - Iter).

of sagittal curvature on saturation must also be considered, as this is a curvature of the fluid-fluid meniscus, not the solid surface.

Figure 10 shows the total, axial and sagittal curvatures at the throat, as a function of saturation, for the volume-of-fluid method. As expected, the total curvature decreases with increasing saturation—the invading phase pressure rises causing the layers to swell toward the center of the pore space, increasing the wetting phase saturation, and the pressure difference between phases reduces, decreasing the capillary pressure. As the capillary pressure decreases, the curvature in the axial plane also decreases. However, it is again evident that the classical assumption of total and axial curvature equivalency is incorrect; the axial curvature is considerably larger than the total curvature for any given saturation. Furthermore, while the total curvatures remain similar for the $\beta = 10°$ and $\beta = 20°$ geometries, the axial curvatures are markedly different, with larger axial curvatures for a given wetting saturation in the 20° sample—this arises as sagittal curvature suppresses the movement of layers in the axial plane.

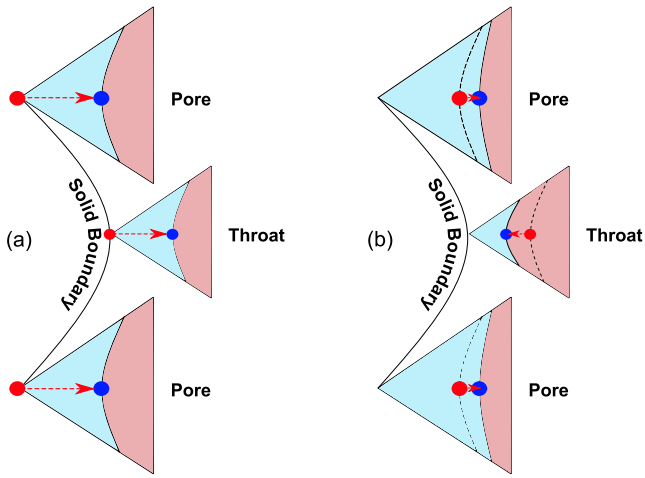

Figure 11. An illustration of the iterative algorithm used to update the sagittal and axial curvatures of a layer interface at the pore (top and bottom) and throat centers (middle). Prior to injection, an initial guess for sagittal curvature is taken using the method described in Section 2.3.2, with the three red points in (a) representing the points used to define the circles in Figures 3a and 3b. Upon injection, the prevailing capillary pressure and initial guess for sagittal curvature are used to determine the axial curvature and hence the location of interface centers, shown by the blue points in (a). Subsequently, the interface centers in (a) comprise the points used to determine the updated sagittal curvature, shown by the red points in (b). In turn, this provides new interface centers, shown by the blue points (b).

A variety of generalized network modeling predictions for saturation and curvature at snap-off are also shown in Figure 10. Without pore or throat sagittal curvature, the GNM threshold curvature predictions reduce to that of a classical network: there is no difference in the threshold total curvature predictions for the two expansion angles; the threshold total curvatures are higher than predicted by direct simulations; and snap-off occurs at far lower wetting saturations than in the direct simulations. If only throat sagittal curvature is included, the GNM's threshold curvature predictions improve dramatically, as shown in Figure 9, but only moderate improvements in wetting saturation at snap-off are observed in Figure 10. While throat sagittal curvature decreases the total curvature necessary for snap-off, allowing larger volumes of wetting phase to occupy the pore space before snap-off occurs, it is the pores which have the largest control over saturation. If pore and throat sagittal curvature are included in the GNM, with optimized coefficients $(c, d) = (1.5, 0.75)$ (Figure C2a), threshold predictions agree well with the direct simulations.

The most interesting finding, however, is that the overall decrease in axial and total curvature predicted by the volume-of-fluid simulations is not linear, but decreases asymptotically until the critical axial curvature for snap-off is reached. This can only occur if the sagittal curvature is not constant. In Figure 10, the sagittal curvature is quantified for both geometries and confirms all previous inferences: the sagittal curvature is negative, smaller in the 10° than the 20° geometry, and increases with increasing saturation, or decreasing capillary pressure. The implication of the latter finding is that sagittal curvature cannot be modeled purely as a function of solid geometry—as hitherto assumed—but rather depends on the morphology of the fluid interfaces.

In Figure 11, the method described in Section 2.3.2 is extended to allow the calculation of sagittal curvature from interface morphology. Initially, layers are assumed to have a sagittal curvature defined by the geometry. A capillary pressure is imposed on the network model which defines the total curvature and, together with the initial sagittal curvature estimate, gives the axial curvature. The centers of the layer interfaces in the axial plane are found and used to define new circles (Figure 11a), from which Equations 7 and 8 provide an updated sagittal curvature. The iterative method is applied throughout the simulation (Figure 11b) to find consistent radial and axial curvatures of the fluid-fluid meniscus; it is the axial curvature which will control when snap-off occurs. Per pressure increment, the method can either be implemented iteratively, or as a single readjustment if the simulation pressure increment is small. The latter approach is used here, as small changes in prevailing capillary pressure allow finer comparison with volume-of-fluid results.

Figure 10 further shows predictions for sagittal curvature, and the total curvature at which snap-off occurs, obtained using the GNM with the extended method of Figure 11, with re-optimized coefficients $(c, d) = (3.5, 3.0)$ (Figure C2b) pertinent to the iterative approach. The semi-analytic approximations in Equation 7 agree well with the direct solutions to Navier-Stokes and Young-Laplace equations, for both geometries. Initially, there is larger disagreement between the sagittal curvatures of the two models due to the GNM reaching lower initial wetting-phase saturations compared to the volume-of-fluid method. Furthermore, the early stages ($\sim S_w = 0.1 - 0.15$) of the direct simulations represent the user-initialized invading phase adjusting into equilibrium with the prevailing capillary pressure. Beyond $S_w = 0.15$, however, the agreement in sagittal curvature is very good, and the total curvature and saturation predictions at snap-off have only minor differences.

3.2. Macroscopic Parameters

The focus of the analysis thus far has been on local parameters. While it is useful to calibrate network models on small samples, where comparison with high-resolution DNS is possible, the real strength of network models lies in their potential to model flow through large domains, with tens-to-hundreds of thousands of pores and throats. Figure 12 evaluates the effect of neglecting, setting a constant, or implementing an iterative sagittal curvature in the GNM on macroscopic capillary pressure and relative permeability predictions. The macroscopic

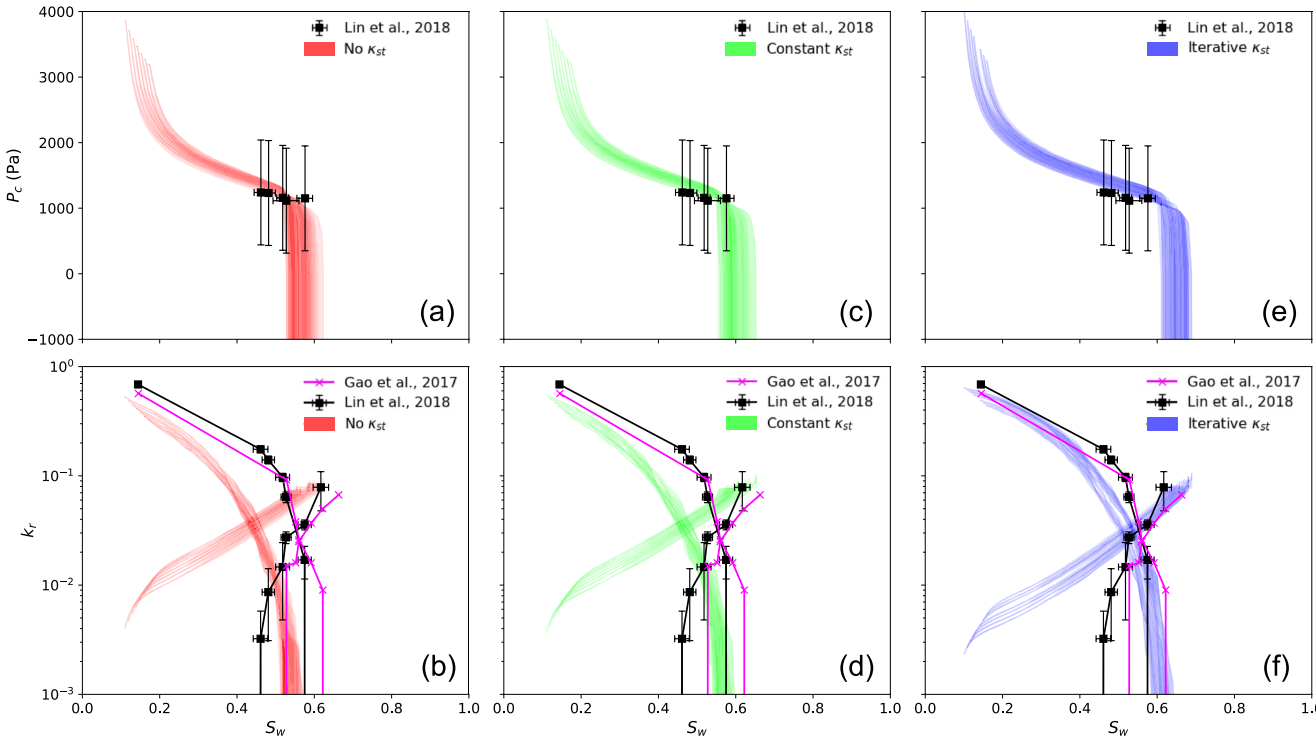

Figure 12. Predicted macroscopic capillary pressures (P_c, top row) and relative permeabilities (k_r, bottom row) for a water-wet Bentheimer sandstone using the GNM. Predictions obtained by neglecting sagittal curvature (red) are shown in (a) and (b), whilst (c) and (d) show a constant sagittal curvature (green). Figures (e) and (f) present GNM predictions using an iterative method (blue) to determine sagittal curvature throughout the simulation. The shaded areas represent the GNM's sensitivity to contact angle, θ, and initial water saturation, S_{wi}: in each figure, GNM simulations span the range defined by $S_{wi} = 0.14 \pm 0.03$ and $\theta = 48° \pm 5°$. The black and magenta lines are pore-scale experimental results by Lin et al. (2018) and Gao et al. (2017), respectively, and the error bars on the experimental capillary pressure and relative permeability values indicate uncertainties in the measurements (Foroughi et al., 2020).

parameter predictions, acquired for a network extracted from a $1{,}000^3$ voxel image of a water-wet Bentheimer sandstone, are compared to experimental measurements of oil-water two-phase flow during waterflooding (Gao et al., 2017; Lin et al., 2018). The shaded areas in Figure 12 represent all GNM predictions using a single value of contact angle assigned in the range [43°, 53°], and an initial water saturation after primary drainage in the range [0.11, 0.17]. These ranges correspond to the experimental measurements and associated uncertainties of thermodynamic contact angle (Blunt et al., 2019) and initial water saturation obtained with differential imaging (Gao et al., 2017). The coefficients of pore and throat sagittal curvature are unchanged from Section 3.1.2 and are described in detail in Appendix C.

While all three approaches produce similar capillary pressure values—which lie within the uncertainty of the experimental measurements—the predicted residual non-wetting saturations are lower if sagittal curvature is included in the GNM (Figures 12a, 12c, and 12e). The variation in residual saturations is also evident in Figures 12b, 12d, and 12f, where significant differences in relative permeabilities can also be seen. If sagittal curvature is completely neglected, snap-off becomes easier and the residual non-wetting saturation increases beyond the range of the experimental measurements (Figure 12b). Furthermore, the experimental measurements of capillary pressure shown in Figures 12a, 12c, and 12e were obtained during the intermediate water fractional flows—imbibition concluded at a wetting saturation $S_w = 0.62$ (Lin et al., 2018), which is under-predicted by the neglection of sagittal curvature in Figure 12a. The exclusion of sagittal curvature can, in part, explain why some studies have struggled to reproduce the capillary trapping behavior of experiments using network models, particularly if low contact angles typical of strongly water-wet systems are assigned to the network (Bondino et al., 2013; Pentland et al., 2010; Raeini et al., 2015; Valvatne & Blunt, 2004). In addition to an over-prediction of residual saturation, as the axial curvature of layer interfaces accommodates the entirety of any capillary pressure decrease, the oil and water relative permeabilities are too low and too high, respectively—for a given pressure the layers are too thick, reducing the conductivity of the phase occupying the center (oil) while increasing the conductivity of the layers (water). The inclusion of constant sagittal curvature, calibrated to replicate volume-of-fluid total

curvature predictions at snap-off (Figure 9), has a noticeable improvement on residual saturations and relative permeabilities, but not to an extent to agree with the experiments (Figure 12d). This is because the absolute value of sagittal curvature at a throat is higher than the value at snap-off for the majority of the experiments, as shown by the DNS results in Figure 10, and so a constant sagittal curvature still overestimates the area of layers in the throat axial plane.

Employing the iterative method, with calibrated throat and pore sagittal curvature as in Figure 10, gives a good agreement between the GNM and experimental results (Figures 12e and 12f). The throat sagittal curvatures are initially large and negative, keeping layers further toward corner vertices and resulting in low initial wetting phase permeabilities. Meanwhile, the center phase occupies a larger cross-sectional area and has a greater permeability than in negligible, or constant, sagittal curvature methods. As the sagittal curvature increases throughout the simulation, the suppression of layer movement in the axial plane lessens, but still results in a far smaller residual than other methods, and overall the effect is a shift in the relative permeabilities and capillary pressures to the right, in agreement with the experiments.

It is further evident from Figures 12b, 12d, and 12f that, whilst the iterative method leads to substantial improvement in oil relative permeability, the water relative permeability at low saturations shows notable discrepancy with experiments across all methods. This is due to two factors: first, the pore-scale experiments in Figure 12 were performed on long, narrow cores with an assumed uniform saturation profile. However, pressure drop estimates from narrow cores are prone to inaccuracies caused by local saturation heterogeneities, leading to erroneously low relative permeabilities (Zhang et al., 2023). Second, PNMs commonly rely on empirical correlations based on two-dimensional finite element predictions to compute center and layer phase conductivity (e.g., Øren et al., 1998; Valvatne & Blunt, 2004). While these correlations provide reasonable predictions, future work could use three-dimensional data-driven methods to obtain more accurate correlations.

3.3. Computational Cost

The improvements in network model predictions achieved through the inclusion of pore-space expansion (Equation 5) and sagittal curvature (Equations 7 and 8) are evident from the results presented in Figures 6, 7, 10, and 12. A key trait of network models, however, is their computational efficiency; any improvements in predictive ability should not sacrifice this efficiency. It is important to note that direct simulations are not required to implement the network model developments presented in this work; DNS were performed solely to measure and improve the accuracy of the approximations on small synthetic systems, while no DNS were performed to obtain the GNM results in Figure 12. The computational costs of the algorithms needed to implement the methods presented in this study scale linearly with network size, which is negligible compared to the cost of determining network permeability, the order of filling and phase connectivity. Thus, the methods presented here offer enhanced physical accuracy with minimal additional cost.

To demonstrate the retention of network model efficiency in the presence of a three-dimensional representation of curvature, the DNS performed on the synthetic geometries in Figures 4 and 5 took approximately 2 weeks using 88 cores in parallel. The GNM simulations performed on the same geometries took less than 5 seconds using a single core on the same machine. Furthermore, Figure 12 represents 63 GNM simulations performed on an image of a real medium. Each simulation, regardless of the curvature method, took approximately 30 min using a single core. The simulations were scheduled to run on 5 cores in parallel, for a total computational time of approximately 6.5 hr. In contrast, a single direct numerical simulation on an image of this size would take on the order of weeks and would require 10 times the computational resources.

4. Conclusions

In this work, a fully three-dimensional characterization of interfacial curvature has been implemented into a network model, which includes the sagittal plane in the computation of displacement capillary pressures. The new expressions for displacement capillary pressures were compared and validated against high resolution volume-of-fluid simulations on synthetic geometries, constructed to vary in their sagittal planes. After validation, the effect on macroscopic capillary pressure and relative permeabilities was analyzed.

Direct simulations demonstrate that neglecting the expansion and contraction of the pore space in a network model gives inaccurate predictions of threshold capillary pressure for piston-like advance. After accounting for

pore-space expansion, the network model results agreed well with direct methods. Additionally, the conventional view of thresholds occurring exactly at pore or throat centers, even for strongly wetted systems, was challenged. The expansion of the pore space necessitates the consideration of intermediate regions as threshold points for displacement in a network model, particularly for contact angles around 90°.

Similarly, the classical assumption that the curvature of fluid interfaces in the sagittal plane is negligible proved incorrect. Direct simulations showed that snap-off predictions differ substantially for systems that are axially identical but vary in their sagittal planes, while quasi two-dimensional approximations employed in CNM were unable to replicate such behavior. Treating curvature in the sagittal plane as a constant property defined by the solid geometry improved the network predictions, but an iterative approach, which considered the exact location of interfaces, more accurately replicated the direct simulations for sagittal curvature.

Macroscopically, sagittal curvature has a large effect on residual saturation and relative permeabilities. Without including sagittal curvature, the network model overestimated the degree of snap-off, and hence residual saturations, and the wetting-phase relative permeability, while underestimating the non-wetting phase relative permeability, compared to experiments. This has important implications for a range of phenomena. For instance, accurate assessment of the efficacy of CO_2 storage relies on predictions of residual saturations. Without including sagittal curvature, overestimates of trapping are inevitable. Likewise, in the construction of fuel cells, it is necessary to design optimum transfer of fluid through the gas diffusion layer and adjacent bipolar plate (e.g., Okonkwo & Otor, 2021; Zhang et al., 2021)—without a consideration of sagittal curvature, relative permeability predictions are likely inaccurate. Similar to local property analysis, the iterative approach to modeling sagittal curvature gave good agreement with experimental results.

Future work could seek to extract the pore-space expansion angles directly from a micro-CT image and to extend the analysis of sagittal curvature to more complex media and wetting states. Current numerical predictions of flow through mixed-wet media are thought to be hindered by an inability to characterize wettability at the pore scale, where terminal interfaces with two distinct planes of curvature have been observed experimentally (Lin et al., 2019; Shojaei et al., 2022). Extending the inclusion of sagittal curvature in network modeling to such scenarios could greatly improve current predictive capabilities.

Appendix A: Piston-Like Curvature Derivation

Figure A1 shows a schematic of a square capillary tube which contracts into the page at an angle β. In the axial plane, shown by Figure A1a, the generalized network model discretizes the square into four corners, shown by the magenta lines defining the coronal planes (Figure A1b) of the pore space. In addition, every corner has a sagittal plane (Figure A1c), shown by the diagonal blue lines in Figure A1a. As a whole, the axial, coronal and sagittal planes retain a three-dimensional description of the pore space used to derive a general equation for piston-like curvature.

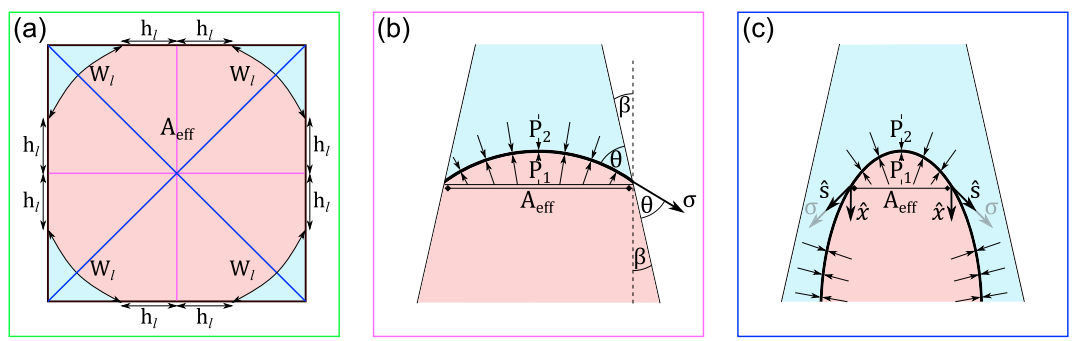

Figure A1. A schematic showing a piston-like interface in a square capillary—which contracts into the page—in the axial (a, green), coronal (b, magenta) and sagittal (c, blue) planes. The piston-like curvature can be derived using a force balance on the interface, where P_1 and P_2 are the invading and receding phase fluid pressures, respectively, β is the expansion angle, θ the contact angle through phase 2, and σ the interfacial tension. The length of the layer interface and invading phase-solid contact length, in each corner, is denoted by W_l and h_l, respectively, while A_{eff} is the effective area of the fluid-fluid interface after it is projected onto the axial plane. In the sagittal plane, an interface tangent vector $\hat{\mathbf{s}}$, is used to determine the component of interfacial tension acting in the vertical direction, given by the vector $\hat{\mathbf{x}}$.

Consider the axial plane shown in Figure A1a. Wetting layers are present in each corner, with a layer interfacial length denoted by W_l. The red, invading phase occupies an effective area of the square, A_{eff}, which contacts the solid perimeter of the square at a length $2h_l$ in every corner.

The fluid-fluid interface is subject to a pressure from the invading and receding phases, shown in the coronal and sagittal planes (Figures A1b and A1c) by P_1 and P_2, which acts everywhere normal to the interface. The resulting vertical force from P_1 and P_2 is obtained by projecting the total area of the interface onto the axial plane (A_{eff} in Figure A1a) and multiplying by the difference in pressure. Additionally, the fluid interface experiences a force from the interfacial tension, σ, acting per unit length along its perimeter and tangent to the interface. Where the invading phase contacts the solid, the interfacial tension acts at an angle $\theta + \beta$ to the vertical (Figure A1b), with θ representing the contact angle. At the layer interfaces, the vector $\hat{\mathbf{s}}$ is tangent to the interface and represents the direction of σ, while $\hat{\mathbf{x}}$ is the direction of the vertical (Figure A1c).

At equilibrium, the sum of forces must balance. Performing a vertical force balance:

$$P_1 A_{eff} = P_2 A_{eff} + \sigma 8 h_l \cos(\theta + \beta) + \sigma 4 W_l \hat{\mathbf{s}} \cdot \hat{\mathbf{x}},$$
$$P_1 - P_2 = P_c = \frac{\sigma(8 h_l \cos(\theta + \beta) + 4 W_l \hat{\mathbf{s}} \cdot \hat{\mathbf{x}})}{A_{eff}}. \tag{A1}$$

Dividing by σ and noting that A_{eff} is given by the difference between the total square and layer area gives an expression for piston-like curvature in the square system. To generalize Equation A1, a summation over every corner belonging to a network element, t, is introduced, where each corner exhibits a fluid-solid length of $2h_l$ and a layer interface length (if present) of W_l, giving:

$$\kappa_{pl} = \frac{\sum_{c \in t}(2 h_l \cos(\theta + \beta) + W_l \hat{\mathbf{s}} \cdot \hat{\mathbf{x}})}{A_{total} - A_{layer}}, \tag{A2}$$

as presented in Section 2.1.1, Equation 4 of this paper.

Appendix B: Snap-Off Curvature Calculation

The following describes the method used to determine sagittal curvature from the volume-of-fluid simulations performed in Section 2.3.2. Consider a corner with half angle γ, shown by the axial plane in Figure B1. If the invading phase, shown in red, has a contact angle θ with satisfies $\theta + \gamma < \frac{\pi}{2}$, then a wetting layer will form.

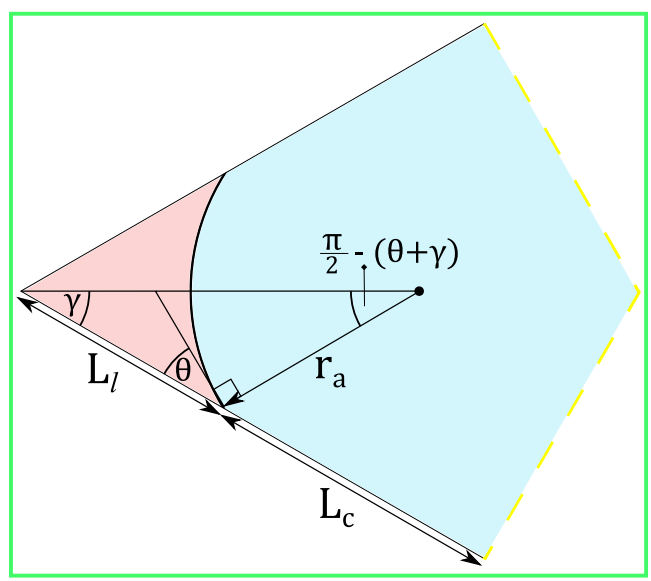

Figure B1. A diagram showing a geometric method to determine the radius of axial curvature, r_a, using the layer-solid and center-solid lengths, L_l and L_c, the corner angle γ and the contact angle measured through the layer, θ.

The length of the layer-solid contact in the axial plane is denoted by L_l, while the center-solid length is L_c. Using simple geometry, the following expression for the axial radius of curvature, r_a, at any L_l, can be derived (Blunt, 2017):

$$\frac{1}{r_a} = \frac{\cos\theta(\cot\gamma - \tan\theta)}{L_l}, \\ = \frac{\cos\theta(\cot\gamma - \tan\theta)}{L_{tot} - L_c}, \tag{B1}$$

where L_{tot} is the theoretical length of the corner side. It is necessary to use L_{tot} and L_c, instead of L_l, to ensure that the smooth corner edges produced during mesh extraction (Figure 5) do not affect the predictions.

The center-solid length is extracted at every simulation time step and Equation B1 is used to determine r_a throughout the simulation. The difference, at the throat, between the total curvature—predicted by the volume-of-fluid simulation's solution to the Laplace equation—and the computed r_a is assigned to the sagittal curvature, r_s (Equation 6).

Appendix C: Optimization of Coefficients

Equation 5 is used to determine the pore-space expansion at every pore center, throat center and half-way point in the network. However, network models are simplified representations of the real pore space: only a coarse resolution is provided by the network extraction process. Physically based approximations of finer details require calibration to mitigate error introduced by spatial simplifications. To optimize the coefficients a and b in Equation 5, the minimum mean absolute difference (Figure C1) between the volume-of-fluid predictions displayed in Figure 6 and the GNM predictions for 225 combinations of a and b is determined using:

$$f(a,b) = \frac{1}{N}\sum_{\theta\in S}\left|{}^{VoF}P_c^{\theta} - {}^{GNM}P_c^{\theta}(a,b)\right|, \tag{C1}$$

where N is the number of contact angles for which predictions exist, ${}^{VoF}P_c^{\theta}$ is the volume-of-fluid threshold capillary pressure prediction at contact angle θ and ${}^{GNM}P_c^{\theta}$ is the GNM threshold capillary pressure prediction at contact angle θ. The summation is over the set, S, of all simulated contact angles. In this work, $N = 9$ and S spans from $\theta = 30°$ to $\theta = 150°$ in 15° increments.

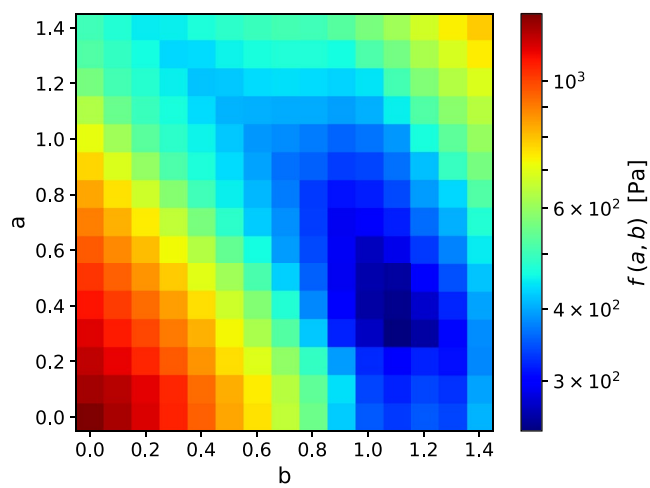

Figure C1. Optimizations performed on the pore-space expansion coefficients a and b present in Equation 5. The mean absolute difference in threshold capillary pressure, $f(a,b)$, between the volume-of-fluid predictions displayed in Figure 6 and the GNM predictions is determined using Equation C1. The combination $a = 0.3$ and $b = 1.1$ corresponds to the global minimum of $f(a,b)$, and these coefficients are maintained for all of the GNM predictions in this work.

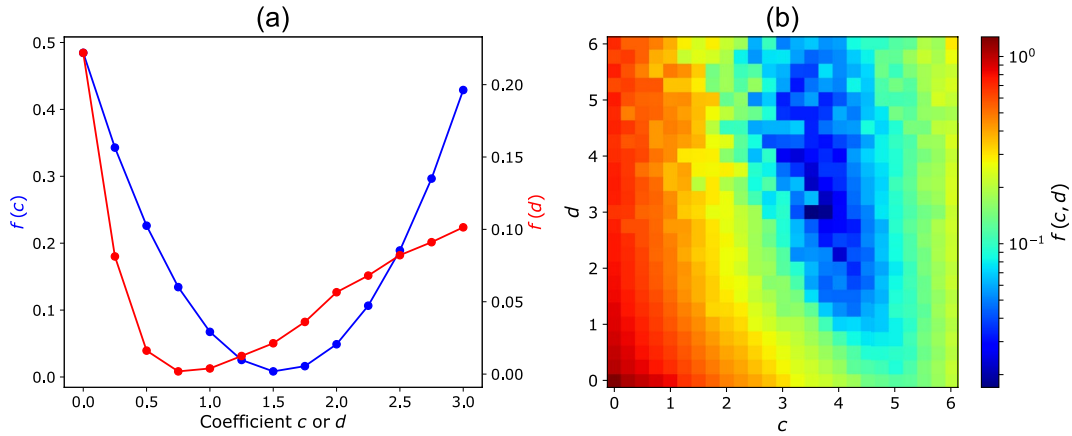

Figure C2. Optimizations performed on the throat sagittal curvature coefficient c and the pore sagittal curvature coefficient d present in Equations 7 and 8, respectively. In (a), the geometry-based throat and pore sagittal curvature are independent of each other and can be optimized by minimizing Equations C2 and C3 separately. In (b), the iterative approach to modeling sagittal curvature results in throat and pore sagittal curvature affecting each other, and the collective objective function in Equation C4 is minimized.

Similar to the treatment of pore-space expansion, the methods to determine sagittal curvature presented in this paper use discrete points defined at the pores and throats. In reality, curvature is mathematically defined at an infinitesimal portion of a surface, and so an estimation using discrete points requires calibration. For the geometry-based method in Figure 3 of Section 2.1.2, the coefficients of throat sagittal curvature (c) and pore sagittal curvature (d) are obtained by minimizing the objective functions:

$$f(c) = \left(1 - \frac{{}^{10}\kappa^{An} + c\,{}^{10}\kappa_{st}}{{}^{10}\kappa^{VoF}}\right)^2 + \left(1 - \frac{{}^{20}\kappa^{An} + c\,{}^{20}\kappa_{st}}{{}^{20}\kappa^{VoF}}\right)^2, \tag{C2}$$

$$f(d) = \left(1 - \frac{{}^{10}S_w(d)}{{}^{10}S_w^{VoF}}\right)^2 + \left(1 - \frac{{}^{20}S_w(d)}{{}^{20}S_w^{VoF}}\right)^2, \tag{C3}$$

where κ^{An} and κ^{VoF} represent two-dimensional analytic solutions and volume-of-fluid predictions of the total curvature at snap-off, respectively, κ_{st} is the throat sagittal curvature obtained from the geometry-based approximation presented in Equation 7, and S_w and S_w^{VoF} denote the throat saturation at snap-off predicted by the GNM and volume-of-fluid method, respectively. In both Equations C2 and C3, the prescripts represent the 10° or 20° geometries in Figure 5. Equations C2 and C3 can be optimized independently as pore sagittal curvature does not affect snap-off curvature at the throat with the geometry-based method, and Equation C2 can be solved analytically. The optimization of c and d is shown in Figure C2a, giving $c = 1.5$ and $d = 0.75$. These coefficients are used to produce the macroscopic results in Figures 12c and 12d.

A consequence of the iterative method to determine sagittal curvature (Figure 11) is that the pores and throats are no longer independent. Therefore, the following objective function is minimized to find the optimal values of the coefficients c and d:

$$f(c,d) = \left(1 - \frac{{}^{10}\kappa(c,d)}{{}^{10}\kappa^{VoF}}\right)^2 + \left(1 - \frac{{}^{20}\kappa(c,d)}{{}^{20}\kappa^{VoF}}\right)^2 + \left(1 - \frac{{}^{10}S_w(c,d)}{{}^{10}S_w^{VoF}}\right)^2 + \left(1 - \frac{{}^{20}S_w(c,d)}{{}^{20}S_w^{VoF}}\right)^2, \tag{C4}$$

where κ represents the total curvature at snap-off predicted by the GNM, and the remaining terms retain their definitions from Equations C2 and C3. Figure C2b shows 625 simulations used to find the global minimum of the objective function in Equation C4, which corresponds to $c = 3.5$ and $d = 3$. These coefficients—which are obtained through calibration against high-resolution direct simulations—are used to produce the macroscopic parameters in Figures 12e and 12f.

Data Availability Statement

The volume-of-fluid model used in this paper is available online at https://github.com/ImperialCollegeLondon/porefoam (Raeini et al., 2012; Shams et al., 2018). The experimental data by Lin et al. (2018) is accessible via the Digital Rocks Portal at https://www.digitalrocksportal.org/projects/157.

Acknowledgments
The authors extend their gratitude to the EPSRC (Grant number EP/R513052/1) for LMG's studentship (project reference 2294896) and Branko Bijeljic is very grateful to TotalEnergies for funding his Senior Fellowship. The authors also thank Mohamed Regaieg, Richard Rivenq and the digital-rock physics team at TotalEnergies for insightful technical discussions.

References

Akai, T., Alhammadi, A. M., Blunt, M. J., & Bijeljic, B. (2019). Modeling oil recovery in mixed-wet rocks: Pore-scale comparison between experiment and simulation. *Transport in Porous Media*, *127*(2), 393–414. https://doi.org/10.1007/s11242-018-1198-8

Alhosani, A., Scanziani, A., Lin, Q., Raeini, A. Q., Bijeljic, B., & Blunt, M. J. (2020). Pore-scale mechanisms of CO_2 storage in oilfields. *Scientific Reports*, *10*(1), 1–9. https://doi.org/10.1038/s41598-020-65416-z

Andrew, M., Bijeljic, B., & Blunt, M. J. (2014). Pore-scale contact angle measurements at reservoir conditions using X-ray microtomography. *Advances in Water Resources*, *68*, 24–31. https://doi.org/10.1016/j.advwatres.2014.02.014

Armstrong, R. T., Porter, M. L., & Wildenschild, D. (2012). Linking pore-scale interfacial curvature to column-scale capillary pressure. *Advances in Water Resources*, *46*, 55–62. https://doi.org/10.1016/j.advwatres.2012.05.009

Bakke, S., & Øren, P.-E. (1997). 3-D pore-scale modelling of sandstones and flow simulations in the pore networks. *SPE Journal*, *2*(2), 136–149. https://doi.org/10.2118/35479-PA

Bear, J., & Cheng, A. H.-D. (2010). *Modeling groundwater flow and contaminant transport* (Vol. 23). Springer Science & Business Media.

Blunt, M. J. (1997). Pore level modeling of the effects of wettability. *SPE Journal*, *2*(4), 494–508. https://doi.org/10.2118/38435-PA

Blunt, M. J. (2017). *Multiphase flow in permeable media: A pore-scale perspective*. Cambridge University Press.

Blunt, M. J., Lin, Q., Akai, T., & Bijeljic, B. (2019). A thermodynamically consistent characterization of wettability in porous media using high-resolution imaging. *Journal of Colloid and Interface Science*, *552*, 59–65. https://doi.org/10.1016/j.jcis.2019.05.026

Bondino, I., Hamon, G., Kallel, W., & Kac, D. (2013). Relative permeabilities from simulation in 3D rock models and equivalent pore networks: Critical review and way forward. *Petrophysics*, *54*(06), 538–546.

Boot-Handford, M. E., Abanades, J. C., Anthony, E. J., Blunt, M. J., Brandani, S., Mac Dowell, N., et al. (2014). Carbon capture and storage update. *Energy & Environmental Science*, *7*(1), 130–189. https://doi.org/10.1039/C3EE42350F

Chatzis, I., & Dullien, F. A. L. (1977). Modelling pore structure by 2-D and 3-D networks with application to sandstones. *Journal of Canadian Petroleum Technology*, *16*(01). https://doi.org/10.2118/77-01-09

Deng, W., Cardenas, M. B., & Bennett, P. C. (2014). Extended roof snap-off for a continuous nonwetting fluid and an example case for supercritical CO_2. *Advances in Water Resources*, *64*, 34–46. https://doi.org/10.1016/j.advwatres.2013.12.001

Diaz, C. E., Chatzis, I., & Dullien, F. A. (1987). Simulation of capillary pressure curves using bond correlated site percolation on a simple cubic network. *Transport in Porous Media*, *2*(3), 215–240. https://doi.org/10.1007/BF00165783

Essaid, H. I., Bekins, B. A., & Cozzarelli, I. M. (2015). Organic contaminant transport and fate in the subsurface: Evolution of knowledge and understanding. *Water Resources Research*, *51*(7), 4861–4902. https://doi.org/10.1002/2015WR017121

Fatt, I. (1956). The network model of porous media. *Transactions of the AIME*, *207*(1), 144–181. https://doi.org/10.2118/574-G

Foroughi, S., Bijeljic, B., & Blunt, M. J. (2021). Pore-by-pore modelling, validation and prediction of waterflooding in oil-wet rocks using dynamic synchrotron data. *Transport in Porous Media*, *138*(2), 285–308. https://doi.org/10.1007/s11242-021-01609-y

Foroughi, S., Bijeljic, B., Lin, Q., Raeini, A. Q., & Blunt, M. J. (2020). Pore-by-pore modeling, analysis, and prediction of two-phase flow in mixed-wet rocks. *Physical Review E*, *102*(2), 23302. https://doi.org/10.1103/PhysRevE.102.023302

Gao, Y., Lin, Q., Bijeljic, B., & Blunt, M. J. (2017). X-ray microtomography of intermittency in multiphase flow at steady state using a differential imaging method. *Water Resources Research*, *53*(12), 10274–10292. https://doi.org/10.1002/2017WR021736

Hall, C. (2009). *Water transport in brick, stone, and concrete* (2nd ed.). CRC Press.

Hassanizadeh, S. M., & Gray, W. G. (1993). Thermodynamic basis of capillary pressure in porous media. *Water Resources Research*, *29*(10), 3389–3405. https://doi.org/10.1029/93WR01495

Jasak, H., Jemcov, A., Tukovic, Z., & others (2007). OpenFOAM: A C++ library for complex physics simulations. *International workshop on coupled methods in numerical dynamics* (Vol. 1000, pp. 1–20).

Jorenush, M. H., & Sepaskhah, A. R. (2003). Modelling capillary rise and soil salinity for shallow saline water table under irrigated and non-irrigated conditions. *Agricultural Water Management*, *61*(2), 125–141. https://doi.org/10.1016/S0378-3774(02)00176-2

Krevor, S., Blunt, M. J., Benson, S. M., Pentland, C. H., Reynolds, C., Al-Menhali, A., & Niu, B. (2015). Capillary trapping for geologic carbon dioxide storage—From pore scale physics to field scale implications. *International Journal of Greenhouse Gas Control*, *40*, 221–237. https://doi.org/10.1016/j.ijggc.2015.04.006

Lenormand, R., Zarcone, C., & Sarr, A. (1983). Mechanisms of the displacement of one fluid by another in a network of capillary ducts. *Journal of Fluid Mechanics*, *135*(-1), 337–353. https://doi.org/10.1017/S0022112083003110

Lerdahl, T. R., Oren, P.-E., & Bakke, S. (2000). A predictive network model for three-phase flow in porous media. In *SPE 5931—Proceedings of the SPEDOE improved oil recovery symposium*. https://doi.org/10.2118/59311-ms

Lin, Q., Bijeljic, B., Berg, S., Pini, R., Blunt, M. J., & Krevor, S. (2019). Minimal surfaces in porous media: Pore-scale imaging of multiphase flow in an altered-wettability Bentheimer sandstone. *Physical Review E*, *99*(6), 1–13. https://doi.org/10.1103/PhysRevE.99.063105

Lin, Q., Bijeljic, B., Pini, R., Blunt, M. J., & Krevor, S. (2018). Imaging and measurement of pore-scale interfacial curvature to determine capillary pressure simultaneously with relative permeability. *Water Resources Research*, *54*(9), 7046–7060. https://doi.org/10.1029/2018WR023214

Maes, J., & Menke, H. P. (2021). GeoChemFoam: Direct modelling of multiphase reactive transport in real pore geometries with equilibrium reactions. *Transport in Porous Media*, *139*(2), 271–299. https://doi.org/10.1007/s11242-021-01661-8

Mason, G., & Morrow, N. R. (1991). Capillary behavior of a perfectly wetting liquid in irregular triangular tubes. *Journal of Colloid and Interface Science*, *141*(1), 262–274. https://doi.org/10.1016/0021-9797(91)90321-X

McClure, J. E., Li, Z., Berrill, M., & Ramstad, T. (2021). The LBPM software package for simulating multiphase flow on digital images of porous rocks. *Computational Geosciences*, *25*(3), 871–895. https://doi.org/10.1007/s10596-020-10028-9

Morrow, N. R. (1970). Physics and thermodynamics of capillary action in porous media. *Industrial & Engineering Chemistry*, *62*(6), 32–56. https://doi.org/10.1021/ie50726a006

Mukherjee, P. P., Kang, Q., & Wang, C. Y. (2011). Pore-scale modeling of two-phase transport in polymer electrolyte fuel cells—Progress and perspective. *Energy & Environmental Science*, *4*(2), 346–369. https://doi.org/10.1039/b926077c

Okonkwo, P. C., & Otor, C. (2021). A review of gas diffusion layer properties and water management in proton exchange membrane fuel cell system. *International Journal of Energy Research*, *45*(3), 3780–3800. https://doi.org/10.1002/er.6227

Øren, P.-E., Bakke, S., & Arntzen, O. J. (1998). Extending predictive capabilities to network models. *SPE Journal*, *3*(4), 324–336. https://doi.org/10.2118/52052-PA

Pan, C., Hilpert, M., & Miller, C. T. (2004). Lattice-Boltzmann simulation of two-phase flow in porous media. *Water Resources Research*, *40*(1), W01501. https://doi.org/10.1029/2003WR002120

Pavuluri, S., Maes, J., Yang, J., Regaieg, M., Moncorgé, A., & Doster, F. (2020). Towards pore network modelling of spontaneous imbibition: Contact angle dependent invasion patterns and the occurrence of dynamic capillary barriers. *Computational Geosciences*, *24*(2), 951–969. https://doi.org/10.1007/s10596-019-09842-7

Pentland, C. H., Tanino, Y., Iglauer, S., & Blunt, M. J. (2010). Capillary trapping in water-wet sandstones: Coreflooding experiments and pore-network modeling. In *SPE 13379—Proceedings of the SPE annual technical conference and exhibition* (Vol. 2, pp. 1245–1253). https://doi.org/10.2118/133798-ms

Prodanović, M., Lindquist, W. B., & Seright, R. S. (2007). 3D image-based characterization of fluid displacement in a Berea core. *Advances in Water Resources*, *30*(2), 214–226. https://doi.org/10.1016/j.advwatres.2005.05.015

Rabbani, H. S., Zhao, B., Juanes, R., & Shokri, N. (2018). Pore geometry control of apparent wetting in porous media. *Scientific Reports*, *8*(1), 1–8. https://doi.org/10.1038/s41598-018-34146-8

Raeini, A. Q., Bijeljic, B., & Blunt, M. J. (2015). Modelling capillary trapping using finite-volume simulation of two-phase flow directly on micro-CT images. *Advances in Water Resources*, *83*, 102–110. https://doi.org/10.1016/j.advwatres.2015.05.008

Raeini, A. Q., Bijeljic, B., & Blunt, M. J. (2017). Generalized network modeling: Network extraction as a coarse-scale discretization of the void space of porous media. *Physical Review E*, *96*(1), 01331. https://doi.org/10.1103/PhysRevE.96.013312

Raeini, A. Q., Bijeljic, B., & Blunt, M. J. (2018). Generalized network modeling of capillary-dominated two-phase flow. *Physical Review E*, *97*(2), 023308. https://doi.org/10.1103/PhysRevE.97.023308

Raeini, A. Q., Blunt, M. J., & Bijeljic, B. (2012). Modelling two-phase flow in porous media at the pore scale using the volume-of-fluid method. *Journal of Computational Physics*, *231*(17), 5653–5668. https://doi.org/10.1016/j.jcp.2012.04.011

Raeini, A. Q., Blunt, M. J., & Bijeljic, B. (2014). Direct simulations of two-phase flow on micro-CT images of porous media and upscaling of pore-scale forces. *Advances in Water Resources*, *74*, 116–126. https://doi.org/10.1016/j.advwatres.2014.08.012

Ramstad, T., Idowu, N., Nardi, C., & Øren, P.-E. (2012). Relative permeability calculations from two-phase flow simulations directly on digital images of porous rocks. *Transport in Porous Media*, *94*(2), 487–504. https://doi.org/10.1007/s11242-011-9877-8

Ruspini, L. C., Farokhpoor, R., & Øren, P. E. (2017). Pore-scale modeling of capillary trapping in water-wet porous media: A new cooperative pore-body filling model. *Advances in Water Resources*, *108*, 1–14. https://doi.org/10.1016/j.advwatres.2017.07.008

Shams, M., Raeini, A. Q., Blunt, M. J., & Bijeljic, B. (2018). A study to investigate viscous coupling effects on the hydraulic conductance of fluid layers in two-phase flow at the pore level. *Journal of Colloid and Interface Science*, *522*, 299–310. https://doi.org/10.1016/j.jcis.2018.03.028

Shojaei, M. J., Bijeljic, B., Zhang, Y., & Blunt, M. J. (2022). Minimal surfaces in porous materials: X-ray image-based measurement of the contact angle and curvature in gas diffusion layers to design optimal performance of fuel cells. *ACS Applied Energy Materials*, *5*(4), 4613–4621. https://doi.org/10.1021/acsaem.2c00023

Silin, D., Tomutsa, L., Benson, S. M., & Patzek, T. W. (2011). Microtomography and pore-scale modeling of two-phase fluid distribution. *Transport in Porous Media*, *86*(2), 495–515. https://doi.org/10.1007/s11242-010-9636-2

Sun, C., McClure, J. E., Mostaghimi, P., Herring, A. L., Shabaninejad, M., Berg, S., & Armstrong, R. T. (2020). Linking continuum-scale state of wetting to pore-scale contact angles in porous media. *Journal of Colloid and Interface Science*, *561*, 173–180. https://doi.org/10.1016/j.jcis.2019.11.105

Valvatne, P. H., & Blunt, M. J. (2004). Predictive pore-scale modeling of two-phase flow in mixed wet media. *Water Resources Research*, *40*(7), W07406. https://doi.org/10.1029/2003WR002627

Wildenschild, D., & Sheppard, A. P. (2013). X-ray imaging and analysis techniques for quantifying pore-scale structure and processes in subsurface porous medium systems. *Advances in Water Resources*, *51*, 217–246. https://doi.org/10.1016/j.advwatres.2012.07.018

Zhang, G., Bao, Z., Xie, B., Wang, Y., & Jiao, K. (2021). Three-dimensional multi-phase simulation of PEM fuel cell considering the full morphology of metal foam flow field. *International Journal of Hydrogen Energy*, *46*(3), 2978–2989. https://doi.org/10.1016/j.ijhydene.2020.05.263

Zhang, G., Foroughi, S., Raeini, A. Q., Blunt, M. J., & Bijeljic, B. (2023). The impact of bimodal pore size distribution and wettability on relative permeability and capillary pressure in a microporous limestone with uncertainty quantification. *Advances in Water Resources*, *171*, 104352. https://doi.org/10.1016/j.advwatres.2022.104352